

# Study of Extreme Magnetopause Distortions under Varying Solar Wind Conditions

Niklas Grimmich<sup>1</sup>, Ferdinand Plaschke<sup>1</sup>, Martin O. Archer<sup>2</sup>, Daniel Heyner<sup>1</sup>,  
Johannes Z. D. Mieth<sup>1</sup>, Rumi Nakamura<sup>3</sup>, David G. Sibeck<sup>4</sup>

<sup>1</sup>Institut für Geophysik und Extraterrestrische Physik, Technische Universität Braunschweig,  
Braunschweig, Germany

<sup>2</sup>Department of Physics, Imperial College London, London, UK

<sup>3</sup>Space Research Institute, Austrian Academy of Sciences, Graz, Austria

<sup>4</sup>NASA Goddard Space Flight Center, Greenbelt, Maryland, US

## Key Points:

- More than 160.000 magnetopause crossings (MPCs) identified in THEMIS data between 2007 and 2022 using a Random Forest Classifier
- MPCs that extremely deviate in location from the Shue et al. (1998) model are quite common
- Important solar wind parameters associated with deviations include the IMF cone angle, solar wind velocity and Alfvén Mach number

---

Corresponding author: Niklas Grimmich, [n.grimmich@tu-braunschweig.de](mailto:n.grimmich@tu-braunschweig.de)

**Abstract**

To first order, the magnetopause (MP) is defined by a pressure balance between the solar wind and the magnetosphere. The boundary moves under the influence of varying solar wind conditions and transient foreshock phenomena, reaching unusually large and small distances from the Earth. We investigate under which solar wind conditions such extreme MP distortions occur. Therefore, we construct a database of magnetopause crossings (MPCs) observed by the THEMIS spacecraft in the years 2007 to mid-2022 using a simple Random Forest Classifier. Roughly 7% of the found crossing events deviate beyond reported errors in the stand-off distance from the Shue et al. (1998) MP model and thus are termed extreme distortions. We find the occurrence of these extreme events in terms of expansion or compression of the MP to be linked to different solar wind parameters, most notably to the IMF magnitude, cone angle, velocity, Alfvén Mach number and temperature. Foreshock transients like hot-flow anomalies and foreshock bubbles could be responsible for extreme magnetospheric expansions. The results should be incorporated into future magnetopause models and may be helpful for the reconstruction of the MP locations out of soft x-ray images, relevant for the upcoming SMILE mission.

**1 Introduction**

Earth’s magnetopause is the boundary layer between the solar wind and the terrestrial magnetosphere. It is an obstacle for the incoming super-magnetosonic solar wind. A bow shock (BS) upstream of the MP decelerates the solar wind and then deflects the plasma around the magnetosphere. The region between the magnetopause and the bow shock is called magnetosheath (e.g., Baumjohann & Treumann, 1997). Depending on the angle between the interplanetary magnetic field (IMF) vector and the bow shock normal, the respective bow shock region (and the magnetosheath) may be denoted as quasi-parallel (angle  $< 45^\circ$ ) or quasi-perpendicular (angle  $> 45^\circ$ ). Upstream of the quasi-parallel bow shock, an extended foreshock region can form, permeated by waves which are excited due to the interaction of the solar wind with particles reflected at and back streaming from the BS (e.g., Eastwood et al., 2005).

Dynamical changes in the solar wind and subsequently in its interaction with the BS influence the magnetosheath flow and impact the MP location and shape. In the absence of reconnection, when the MP can be described as a rotational discontinuity, the MP is well-characterized as a tangential discontinuity at which pressure balance should hold. On the magnetospheric side, the magnetic pressure is the most important contributor to that balance, while on the magnetosheath side dynamic, plasma (thermal) and magnetic pressures (from the draped IMF) contribute significantly (e.g., Shue & Chao, 2013). Thus, variations of the total pressure in the solar wind and in the magnetosheath lead to inward and outward motion of the MP. Additionally, strong southward IMF conditions lead to magnetic flux erosion from the dayside MP via magnetic reconnection and therefore inward motion of the dayside MP (Aubry et al., 1970; Sibeck et al., 1991; Shue et al., 1997, 1998). Solar wind dynamic pressure, IMF strength and orientation and the dipole tilt angle can be identified as the parameters influencing the MP location (Sibeck et al., 1991; Shue et al., 1997; Liu et al., 2012). Consequently, many empirical MP models use the solar wind dynamic pressure  $p_{\text{dyn}}$ , the IMF  $B_z$ -component and in some instances the dipole tilt as input parameters (e.g., Fairfield, 1971; Sibeck et al., 1991; Shue et al., 1997; Chao et al., 2002; Lin et al., 2010; Nguyen et al., 2022c, and many others). In these models, the MP stand-off distance  $R_0$  serves as an indicator for the overall location of the boundary layer.  $R_0$  is often strongly dependent on one or both of the two parameters  $p_{\text{dyn}}$  and  $B_z$ .

Newer models like the one from Lin et al. (2010) or Nguyen et al. (2022c) use additional parameters like the solar wind magnetic pressure and the dipole tilt to take asymmetries and cusp indentation into account, enhancing the forecasting accuracy of the model,

e.g., shown by Case and Wild (2013) for the Lin et al. (2010) model. Physics-based MHD models like, e.g., Liu et al. (2015) include all IMF components,  $P_{\text{dyn}}$  and the dipole tilt as parameters to give an even better forecasting accuracy under normal solar wind conditions. Nevertheless, most models fail to predict magnetopause locations under extreme pressure conditions (e.g., Tátrallyay et al., 2012; Suvorova & Dmitriev, 2015). In these cases, other parameters can become more significant. One of those parameters, which to our knowledge is not included in the models and also describes the IMF orientation, is the IMF cone angle  $\vartheta_{\text{cone}}$  between the Earth-Sun-line and the IMF vector. Magnetospheric expansions beyond the magnetopause model predictions are often found when the IMF is quasi-radial ( $\vartheta_{\text{cone}} < 30^\circ$ ) (Fairfield et al., 1990; Suvorova et al., 2010; Dušík et al., 2010; Samsonov et al., 2012; Grygorov et al., 2017). Another parameter could be the IMF clock angle  $\vartheta_{\text{cone}}$  between IMF  $B_y$ - and  $B_z$ -components, as Lu et al. (2013) showed in global MHD simulations, that the IMF  $B_y$  and  $B_z$  components might have influence on the MP shape.

In addition to changes in the dynamic pressure and/or IMF orientation, other phenomena have been discussed as origins of MP disturbances, which can lead to extreme  $R_0$  values. Phenomena originating near the magnetopause include magnetic reconnection and associated flux transfer events (FTE, e.g., Elphic, 1995) or the Kelvin-Helmholtz instability (KHI, e.g., Johnson et al., 2014). In the magnetosheath, so called magnetosheath or high-speed jets (HSJs) can travel from their point of origin at the bow shock down to the magnetopause and cause an indentation and excitation of surface waves (Shue et al., 2009; Plaschke et al., 2018; Archer et al., 2019). Finally, kinetic transients in the foreshock region, like hot-flow anomalies (HFAs) or foreshock bubbles (FBs) and ULF-wave generated phenomena like foreshock cavitons, short large-amplitude magnetic structures (SLAMS) or shocklets, can impact the MP in different ways as well (Sibeck et al., 1999; Jacobsen et al., 2009; Turner et al., 2011; Archer et al., 2015; H. Zhang et al., 2022). Some of these phenomena only result in localized distortions (e.g. HFAs, Sibeck et al., 1999; Turner et al., 2011), others could have global impacts (e.g. FBs, Archer et al., 2015).

These phenomena and the solar wind-magnetosphere interactions have been studied for two decades using data from several multi-spacecraft missions. Cluster (Escoubert et al., 2001) contributed significantly to the exploration of different plasma regions of the magnetosphere, advancing our understanding of reconnection and the movement of the magnetopause (see Haaland et al., 2021, for a comprehensive overview). The Time History of Events and Macro-scale Interactions during Substorms (THEMIS) mission (Angelopoulos, 2008) enabled observations of solar wind phenomena and direct responses in the magnetosphere due to the special orbit configuration of the multiple spacecraft. The aim of the most recent mission MMS is to study in detail magnetic reconnection at the smallest scales (Burch et al., 2016).

Typically, all these spacecraft can only observe the MP at the position and time they cross this boundary or when the MP is in motion and moves over the spacecraft. So far, global observations of the MP have not been possible. The upcoming Solar Wind Magnetosphere Ionosphere Link Explorer (SMILE) mission will provide the first opportunity to observe the location, shape and motion of the dayside MP at any given time (Raab et al., 2016; Branduardi-Raymont et al., 2018), based on measurements of soft x-rays. Soft x-rays are emitted during solar wind charge exchange with neutrals from the Earth's exosphere (e.g., see review by Kuntz, 2019). Studies of this phenomenon in the near-Earth regions showed the possibility to image the magnetospheric boundary layers in soft x-ray wavelengths and reconstruct the magnetopause surface from the images (e.g., Sibeck et al., 2018; C. Wang & Sun, 2022). SMILE will take advantage of this to study the whole dayside magnetosphere from a polar orbit and image the soft x-rays with a Soft X-ray Imager (SXI) to track the magnetopause motion on global scales. Additional instrumentation of SMILE will include a Magnetometer (MAG), a Light Ion Analyser (LIA) and an Ultra-Violet Imager (UVI) which will monitor the plasma environment,

121 in particular the solar wind conditions, and the auroral oval in UV wavelengths, respec-  
 122 tively. Thereby, the motion of the magnetopause can be linked to the upstream plasma  
 123 conditions and the ionospheric response.

124 The SMILE mission is expected to launch in late 2024 or early 2025. In prepara-  
 125 tion, much effort is put into the development of MP reconstruction techniques based on  
 126 simulated SXI images, for which fundamental knowledge about the magnetopause shape  
 127 and behaviour is needed (see C. Wang & Sun, 2022, and references therein). The influ-  
 128 ence of IMF parameters on it has been subject to several statistical studies (e.g., Plaschke,  
 129 Glassmeier, Auster, Angelopoulos, et al., 2009; Dušík et al., 2010; Staples et al., 2020;  
 130 Nguyen et al., 2022b). In this study, we focus on extreme MP locations, which cannot  
 131 be explained with a common MP model like the improved Shue et al. (1998) model, the-  
 132oretically capable of predicting the MP location under extreme solar wind conditions.  
 133 The reason for this is most likely due to the fact that such models are designed to be op-  
 134 timal around the typical conditions and give an average location and shape of the MP.  
 135 Therefore, extreme and unusual conditions are given less weight in fitting the models,  
 136 resulting in model predictions deviating under such conditions.

137 In previous works extreme MP locations were often only studied on a case by case  
 138 bases. Utilizing multiple years of THEMIS data we can construct a large database of cross-  
 139 ing events and study the extreme and unusual MP locations with a statistical approach.  
 140 In particular, we are interested under which solar wind conditions these events occur.  
 141 Understanding the origins of extreme MP locations, which might be parameters included  
 142 in other models or extreme conditions, will help improve future models and help under-  
 143 stand the interaction between the solar wind and the magnetosphere in more detail. In  
 144 the following, we give a brief introduction to the used spacecraft data (section 2). We  
 145 describe the construction of our database of magnetopause crossings observed by the THEMIS  
 146 spacecraft (section 3) and show the results (section 4). We then compare the solar wind  
 147 conditions for which extreme events occur with the standard solar wind distributions (sec-  
 148 tion 5). Eventually, we discuss and summarize our findings (section 6).

## 149 2 Spacecraft Data

150 Since 2007 the spacecraft of the THEMIS mission have been orbiting Earth near  
 151 the equatorial plane to investigate the plasma environment in the near-Earth region (Angelopoulos,  
 152 2008). For the identification of MPCs in the timespan of 2007 to 2022, we use the mag-  
 153 netic field data from the Fluxgate Magnetometer (FGM, Auster et al., 2008), and par-  
 154 ticle data and moments from the Electrostatic Analyzer (ESA, McFadden et al., 2008).  
 155 Data from the entire 15 years interval are used from probes THA, THD, and THE, while  
 156 THB and THC only contribute data until the end of 2009, as they were then sent into  
 157 lunar orbits, becoming the ARTEMIS mission (Angelopoulos, 2011).

158 FGM and ESA data are used in the spin-resolution (FGM) and reduced mode (ESA)  
 159 with cadences of about 3 to 4 s. Low resolution FGM data and full mode ESA data are  
 160 used to bridge bigger data gaps ( $> 15$  min) (see data treatment by Nguyen et al., 2022a).  
 161 This occurs almost exclusively in the velocity data of ESA, leading to some uncertain-  
 162 ties in this data which can be compensated in our detection method. The FGM and ESA  
 163 data are synchronized and resampled to common 3 s time stamps. Finally, we average  
 164 the data in a moving 60 s window for each time step, to smooth out turbulent fluctu-  
 165 ations which could be misidentified as MPCs. The data is processed in 1-hour intervals  
 166 with an overlap of 2 minutes into the next interval. Intervals were omitted for data gaps  
 167 that could not be bridged, i.e. if less than 15 mins of data were available in both the high  
 168 and low resolution. This is necessary, as large data gaps lead to jumps in the data which  
 169 could be misinterpreted as MPCs. Results are combined to a bigger dataset afterwards.

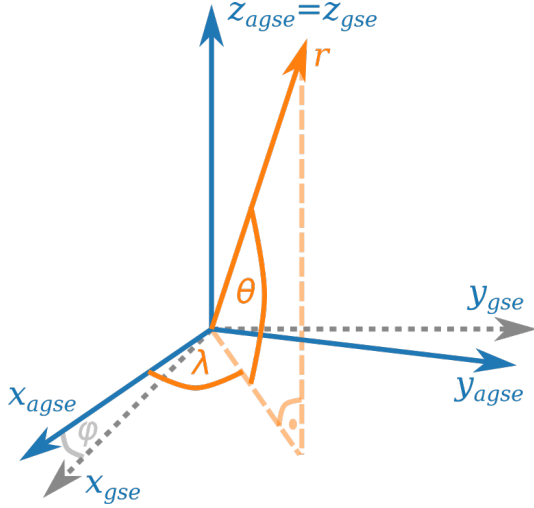


**Figure 1.** Orientations and relations of the two main coordinate systems. The grey axes depict the standard GSE (geocentric solar ecliptic) system. The cartesian and spherical AGSE (aberrated geocentric solar ecliptic) coordinate axes are depicted in blue and orange, respectively.

170 All vector quantities in the dataset are transformed into the AGSE (aberrated geo-  
 171 centric solar ecliptic) coordinate system with an average aberration angle of  $\varphi \sim 4.3^\circ$   
 172 resulting from the Earth's orbital velocity of 30 km/s around the Sun and an average  
 173 solar wind speed of 400 km/s. Taking this aberration effect on the MP into account, im-  
 174 proves the prediction of MP models (e.g., Safránková et al., 2002).

175 We limit our investigation to the dayside magnetosphere (position in AGSE x-direction  
 176 larger than 0) outside the nominal plasmasphere (minimal radial distance from the Earth's  
 177 center larger than  $4 R_E$ ). These conditions have to be fulfilled throughout the 1-hour  
 178 intervals. This can result in fewer observations near the terminator.

179 In addition to the observational data, we construct a dataset containing the orbital  
 180 data of the THEMIS probes in the cartesian ( $x, y, z$ ) and the spherical AGSE coordinates  
 181 ( $r, \theta, \lambda$ , see Fig. 1) in 1-minute resolution for the all selected time intervals. This dataset  
 182 also comprises the equivalent stand-off distance  $R_{0,sc}$  calculated with the Shue et al. (1997,  
 183 1998), hereafter SH98, model equation, as done in previous studies (Plaschke, Glassmeier,  
 184 Auster, Constantinescu, et al., 2009; Plaschke, Glassmeier, Auster, Angelopoulos, et al.,  
 185 2009; Staples et al., 2020):

$$186 \quad R_{0,sc} = r \left( \frac{2}{1 + \cos \zeta} \right)^{-\alpha}. \quad (1)$$

187 Here  $r$  is the radial distance from the Earth's center to the spacecraft and  $\zeta$  is the zenith  
 188 angle between the  $x$ -axis and the Earth-spacecraft-line (denoted by  $\theta$  in Shue et al., 1997,  
 189 1998). The flaring parameter  $\alpha$  is calculated with the formula given by Shue et al. (1998),  
 190 using the appropriate dynamic solar wind pressure  $p_{dyn}$  and IMF component  $B_{z,IMF}$  for  
 191 all orbital points:

$$192 \quad \alpha = \left( 0.58 - 0.007 \frac{B_{z,IMF}}{\text{nT}} \right) \left[ 1 + 0.024 \ln \left( \frac{p_{dyn}}{\text{nPa}} \right) \right]. \quad (2)$$

193 We take into account that our approximation of a static solar wind speed for the  
 194 aberration effect results in mean errors of  $0.034 R_E$  for  $R_{0,sc}$  and  $0.823^\circ$  for the longitude-  
 195 position, which have no drastic influence on our study. To calculate the presented errors,

196 we average the differences between position values of THEMIS adjusted with a dynamic  
197 solar wind and with a static solar wind aberration.

198 The appropriate solar wind parameters are obtained from the high resolution 1-  
199 min OMNI dataset, which mainly combines the WIND (Lepping et al., 1995; Ogilvie et  
200 al., 1995) and ACE (Stone et al., 1998; Smith et al., 1998; McComas et al., 1998) space-  
201 craft data, time-shifted to the bow shock nose (see King & Papitashvili, 2005, for details  
202 on the shift technique). Smaller data gaps up to 5 minutes in the OMNI dataset are bridged  
203 by linear interpolation.

### 204 3 Magnetopause Crossing Identification Method

205 Our identification process utilizes a combination of supervised machine learning  
206 methods and a threshold-based classification, to infer crossing events from automatically  
207 labelled data.

208 Recent studies have already shown the efficiency of classifying the near-Earth re-  
209 gions from spacecraft data with machine learning methods (e.g., Breuillard et al., 2020;  
210 Olshevsky et al., 2021; Nguyen et al., 2022a). In particular Nguyen et al. (2022a) showed  
211 that even a simple machine learning algorithm like the Gradient Boosting Classifier can  
212 outperform manually set threshold based detection methods of the three typical near-  
213 Earth regions (solar wind, magnetosheath and magnetosphere), reaching more than sat-  
214 isfying accuracies.

215 Unfortunately, Nguyen et al. (2022a) only inferred if one MPC is found in a 1-hour  
216 interval, finding only a limited amount of MPCs with an uncertain location. This is not  
217 suitable for our study, as we can not be certain to infer the right model deviations from  
218 their catalogue. We aim to construct a database in which extreme MPCs are clearly iden-  
219 tified on smaller timescales and with a clear spacecraft location, which can be used in  
220 future studies on extreme MP distortions. Nevertheless, we can use the same approach  
221 as Nguyen et al. (2022a) in giving every data point a label according to the near-Earth  
222 region it most likely pertains to, and then infer the boundary crossings from the labels.  
223 For our study, we only need to distinguish between data points that are in the magne-  
224 tosphere labelled 1 and data points that are not in the magnetosphere labelled 0, facil-  
225 itating the identification of magnetopause crossings.

226 In Fig. 2 we present a flow diagram summarizing our identification process. De-  
227 tailed description can be found in the following sections.

#### 228 3.1 Machine Learning Algorithms

229 For our study, we only need to distinguish between data points that are in the mag-  
230 netosphere labelled 1 and data points that are not in the magnetosphere labelled 0, fa-  
231 cilitating the identification of magnetopause crossings.

232 Nguyen et al. (2022a) trained their algorithm with data resampled to 1-minute res-  
233 olution consisting of the magnetic field components ( $B_x$ ,  $B_y$ ,  $B_z$ ), the ion velocity ( $v_x$ ,  $v_y$ ,  $v_z$ ),  
234 the ion density  $n_{\text{ion}}$  and the ion temperature  $T_{\text{ion}}$ . We include the magnitude of mag-  
235 netic field and velocity as well as a flux index  $F_{\text{idx}}(t)$  which describes the omnidirectional  
236 energy flux of ions with energies between  $10^2$  eV and  $10^4$  eV, where the solar wind and  
237 magnetosheath regions are easily identified:

$$238 F_{\text{idx}}^{1e2,1e4}(t) = \log_{10} \left( \int_{10^2 \text{ eV}}^{10^4 \text{ eV}} \frac{E_{\text{Flux}}(t)}{\frac{\text{eV}}{\text{cm}^2 \cdot \text{s} \cdot \text{sr}}} dE \right). \quad (3)$$

239 The index reaches high values of 10 and above if the magnetosheath ion population is  
240 observed, otherwise  $F_{\text{idx}} < 10$  holds (compare panels (5) and (6) of Fig. 3). This  $F_{\text{idx}}(t)$

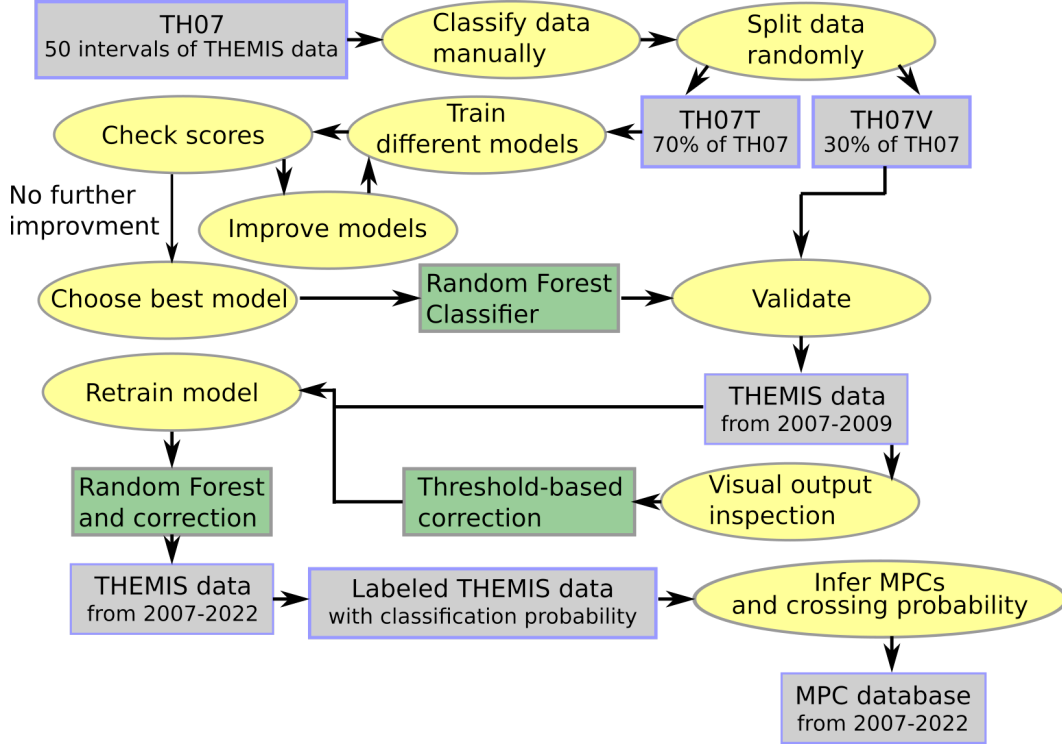


**Figure 2.** Flow diagram outlining our identification process.

241 can be better handled by the model than the total energy flux distribution for each time  
 242 step.

243 To train and compare different machine learning algorithms, we built a dataset of  
 244 50 randomly selected time intervals with different lengths of the initial phase of the THEMIS  
 245 mission in 2007 (TH07), that represent well outer-magnetospheric dayside observations  
 246 (see Fig. 4). Each interval contains at least one magnetopause crossing. All data points  
 247 are then labelled manually by visually inspecting  $n_{\text{ion}}$  and  $B_z$  changes, as well as ion en-  
 248 ergy flux density measurements, yielding roughly 30,000 labelled data points from in-  
 249 side (Label 1) and outside (Label 0) the magnetosphere with  $\sim 1300$  MPCs for train-  
 250 ing. Data points in a smeared out MPC or boundary layer are attempted to be separated  
 251 in the middle of the crossing. Fig. 3 displays one of the intervals from TH07 with all in-  
 252 put parameters for the algorithms; it also shows labels given manually and by the trained  
 253 Random Forest machine learning classifier.

254 We randomly divide our dataset TH07 into a training set (70% of the data points,  
 255 TH07T) and a validation set (30% of data points, TH07V). With TH07T we train, test  
 256 and compare different models to decide which model to utilize for the identification. TH07V  
 257 is later used to verify the training scores of the best model, assuring the model has not  
 258 overfitted the trainings data. The nature of our problem, inside (class/label 1) or out-  
 259 side (class/label 0) the magnetosphere, is a binary classification problem which can be  
 260 tackled with a number of different algorithms (e.g., described in Géron, 2019).

261 One of the simplest binary classifiers is the Logistic Regression (LR, e.g., Cox &  
 262 Snell, 1970), predicting the probability of a data point belonging to the positive class (la-  
 263 bel 1) by calculating a logistic (sigmoid) function of a linear fit of the input data. This  
 264 algorithm assumes that the data points are linearly distributed in parameter space. Ad-  
 265 ditionally, the data has to be normalized for the algorithm to work properly.

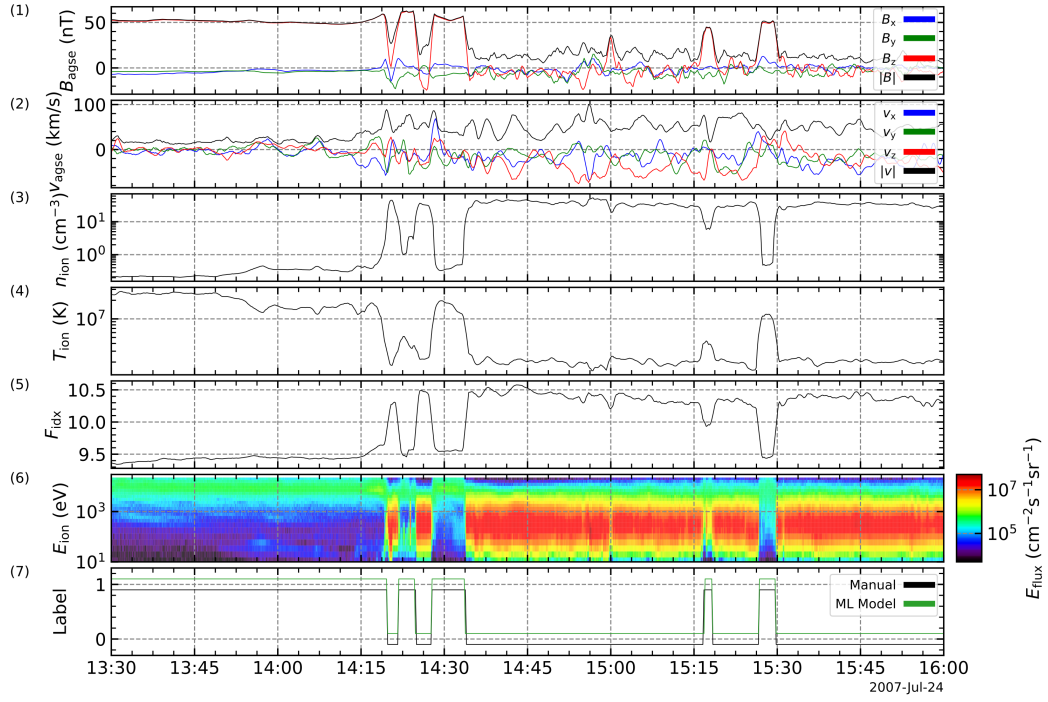


**Figure 3.** Time series plot of THEMIS data (THE) on the 24 July 2007. From top to bottom the panels display the averaged magnetic field data, the ion velocity, the ion density, the ion temperature, the energy flux density, the flux index and the data label given manually and by a Random Forest Classifier. The label values were shifted slightly for better visual comparison.

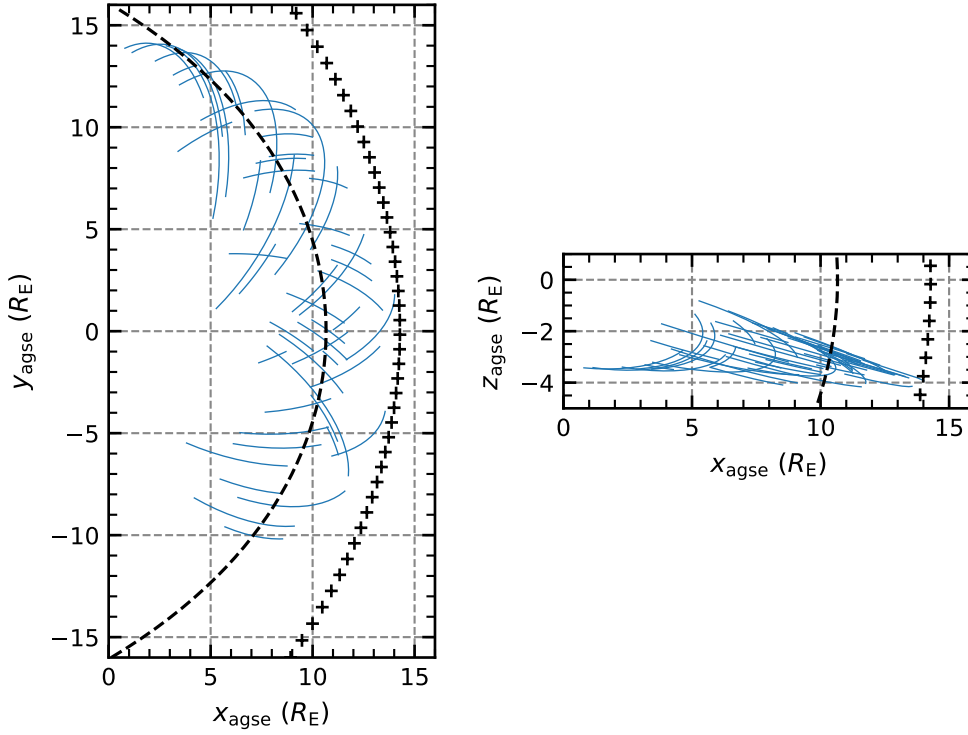


**Figure 4.** Spatial distribution of 50 training intervals in the AGSE x-y-plane (left panel) and x-z-plane (right panel), respectively. The dashed line represents the Shue et al. (1998) model magnetopause and the black crosses represent the Chao et al. (2002) model bow shock for  $B_{z,\text{IMF}} = -1$  nT and  $p_{\text{dyn}} = 1.5$  nPa.

Another often used method is the Decision Tree (DT, e.g., Breiman et al., 1984). This algorithm can directly (with only little preprocessing) predict a class from different input data using simple if-then-else decision rules inferred from data features/input parameters. A common problem with DTs, if not restricted correctly, is overfitting, i.e., adapting too tightly to the training data, reducing the adaptability of the model to new data.

More advanced algorithms like the Random Forest (RF, e.g., Breiman, 2001) or Gradient Boosting (GB, e.g., Friedman, 2001) use ensemble methods for their prediction: multiple simple models are trained on the data and the final prediction are then derived from the predictions of all contributing simple models. Both RF and GB algorithms use DTs as basis. The RF algorithm trains a group of DTs on random training data subsets and use the most common prediction in the group as final prediction, therefore reducing the problem of overfitting of the individual DTs. The GB on the other hand sequentially fit DTs on the residual errors of the previously trained DT until the ensemble converges on the smallest errors, and predicts the class via the sum of the ensemble predictions. These ensemble methods are widely used in many machine learning applications, reaching high accuracies (Géron, 2019). Nguyen et al. (2022a) used the GB algorithm in their work for the identification of the near-Earth regions in spacecraft data.

All the presented algorithms, except the RF, were also compared by Nguyen et al. (2022a). We start the training with more input parameters, hence, we repeat the model comparison here to ensure using the optimal model. For the comparison we have to split our training data TH07T again into training subset (TH07TC) and into a validation subset (TH07TV) with a data ratio of 70/30.

For the first testing round, we utilize the default implementation of the algorithms from Python's Scikit-learn library (Pedregosa et al., 2011) and evaluate the models via the cross validation (CV) scores. Cross validation means that the training data (TH07TC) is split into  $n$  equally sized subsets. The model is then trained and evaluated  $n$  times with all possible combinations of these subsets as training ( $n-1$  subsets) and validation data (1 subset). Thus, the CV scores give us a mean accuracy (fraction of correct predictions) and standard deviation over all  $n$  subsets, working as an indicator for the independence of the data split into training and validation data. Here we utilize a 10-folded CV, i.e., we split the TH07TC into  $n=10$  subsets. Based on this first CV, we can already conclude that the two ensemble classifiers perform better. Nevertheless, as suggested by Géron (2019), we aim at improving all the models by adjusting some important hyperparameters (specific boundaries for the algorithms) using a grid search method: We train and evaluate the models via CV with different parameter combinations in search for the best scores.

In the case of the LR the default hyperparameters yield the best results, while for the other algorithms the grid search shows that setting hyperparameters like the maximal tree depth and the number of estimators (here: DTs) in the ensemble resulted in better scores. The maximal tree depth limits the number of if-then-else decisions in the DTs, reducing the risk of overfitting the models. The best results are obtained by setting the parameters as follows: for the simple DT the maximal depth is set to 20, for the RF it is set to 40 and for the GB it is set to 15. The number of estimators is set to 600 and 400 for the RF and GB classifier, respectively. Additionally, the learning rate in the GB classifier is changed from 0.1 to 0.5, i.e., the fitting of the base estimators is accelerated slightly, without risking overfitting, by setting a higher number of estimators.

In addition to the CV score, we look at other scores that are often used for validating (binary) classifiers (Géron, 2019): the precision is the ratio of correct predictions out of all *inside magnetosphere* algorithm predictions; the recall or sensitivity is the ratio of correct predictions out of all true *inside* labels. For example, a recall of 0.95 for

**Table 1.** Final validation scores of different ML algorithms.

Score	Logistic Regression	Decision Tree	Random Forest	Gradient Boosting
CV	$0.9633 \pm 0.0012$	$0.9877 \pm 0.0007$	$0.9939 \pm 0.0005$	$0.9937 \pm 0.0005$
Precision	0.9606	0.9889	0.9939	0.9937
Recall	0.9722	0.9882	0.9938	0.9938
AUC	0.9944	0.9881	0.9998	0.9998

317 a classifier means that 95% of the data points inside the magnetosphere are predicted  
318 correctly.

319 To ascertain which model can distinguish best between the two classes, we also uti-  
320 lize the AUC (area under the curve) score. This score is derived as the integral from the  
321 receiver operating characteristic (ROC) curve, which describes the true positive rate (which  
322 is identical to the recall) as a function of the false positive rate (ratio of false predictions  
323 out of all true *outside* labels). For a purely random classifier, the AUC score would be  
324 0.5, while a value of 1 would indicate a classifier perfectly distinguishing between the two  
325 classes.

326 The final validation scores for the algorithms are obtained by application of the trained  
327 models on the validation set TH07TV (after the setting of the hyperparameters accord-  
328 ing to the results of the grid search discussed above); They are depicted in Table 1. As  
329 can be seen, all algorithms share scores with values over 0.96 in all categories, and there-  
330 fore could distinguish between the two classes and predict many magnetospheric data  
331 points correctly. By looking at the different scores in detail, it's clear that the DT per-  
332 forms better than the LR in regard to CV score, precision and recall; only in the AUC  
333 score LR shows higher values. Overall, the ensemble methods (RF and GB) perform even  
334 better than the simpler models, yielding nearly identical scores. The CV scores show the  
335 lowest standard deviation of  $5 \cdot 10^{-4}$ . Higher accuracies of 0.994 indicate a slightly bet-  
336 ter independence from the chosen training data. RF and GB also have precisions and  
337 recalls over 0.994 and AUC scores of 0.999. Thus, the ensemble methods are slightly bet-  
338 ter suited for the classification: they can distinguish very well between the two classes  
339 while also correctly predicting the labels in over 99% of the cases, matching the model  
340 comparison results of Nguyen et al. (2022a).

341 Finally, we compared the feature/input parameter importance of the RF and GB  
342 classifiers for the prediction of data points. The feature importance is a calculation of  
343 the relative contribution of each feature to the final decision, showing easily the influ-  
344 ence of parameters to the model results. While the GB classifier mainly utilizes the ion  
345 density for its prediction, the RF uses many of the input parameters in its decision. This  
346 leads to the RF classifier being not as much affected by spurious density changes as the  
347 GB classifier; the latter tends to label density peaks erroneously as magnetosheath data,  
348 even if other observations suggested a different classification.

349 Thus, we decide to utilize the RF classifier to label the THEMIS data. We train  
350 it on our complete training dataset TH07T. The previous obtained scores are again ver-  
351 ified by validating the RF classifier on the validation set TH07V.

### 352 3.2 Additional Threshold-based Corrections

353 Visual inspection of  $\sim 100$  randomly selected intervals from 2007 to 2009 that were  
354 labelled with the Random Forest Classifier revealed some identification mistakes asso-  
355 ciated with foreshock phenomena or BS crossings. In addition, some mistakes were also

found related to cold plasma observations deep inside the magnetosphere. To correct these mistakes, we use the following threshold-based label correction:

1. Southward IMF ( $B_z \leq 0$  nT) and large ion velocities in AGSE x-direction ( $v_x \leq -250$  km/s) should only be observed outside the dayside magnetosphere. If either (or both) of these criteria is fulfilled and if, in addition, ion densities above  $n_{\text{ion}} > 0.5$  cm $^{-3}$  are observed, then the associated points are relabelled as outside the magnetosphere.
2. High magnetic field magnitudes ( $B > 150$  nT) and small deviations between the flux index and a high energy flux index ( $F_{\text{idX}}^{1e2,1e4} - F_{\text{idX}}^{6.5e3,1e4} \leq 0.5$ ) should only be observed inside the magnetosphere. If either (or both) of these criteria is fulfilled and if, in addition, ion densities below  $n_{\text{ion}} < 0.75$  cm $^{-3}$  are observed, then the associated points are relabelled as inside the magnetosphere.

Roughly one percent of the labels have been corrected. The classification probability of these corrected labels is manually set to 0.85, indicating the correction.

We retrain our model on the gathered dataset of THEMIS data between 2007 and 2009 with corrected labels, trying to improve the classifier with these new labels. From here on, since directly adjacent points often share the same label, we choose a new data sampling rate of 12 s. Hence, we could accelerate the classification process without losing the accuracy of our model. Then we utilize the retrained Random Forest Classifier to label the remaining data up to 2022, while also applying the threshold-based label correction for 1% of the data.

### 3.3 Identification of Magnetopause Crossings

We search for MPCs by automatically identifying the times where labels change from one region to the other. We only count a label change as a MPC if at least two points before and after the change belong to the same region. That means a spacecraft has to be at least 24 s in a different region for a crossing to count.

The identification process results in an average of 13,164 MPCs per year. In total, 184,292 MPCs have been observed by the THEMIS spacecraft over the 15 years studied. These MPCs are collected into the dataset TH-MPC (Grimmich et al., 2023)

We calculate the deviation from the theoretical model stand-off distance  $\Delta R_0$  given by the SH98 model for each identified crossing

$$\Delta R_0 = R_{0,\text{sc}} - R_{0,\text{Shue}}, \quad (4)$$

$$R_{0,\text{Shue}} = \left[ 10.22 + 1.29 \tanh \left( 0.184 \left( \frac{B_{z,\text{IMF}}}{\text{nT}} + 8.14 \right) \right) \right] \left( \frac{p_{\text{dyn}}}{\text{nPa}} \right)^{-\frac{1}{6.6}}, \quad (5)$$

where equation (5) corresponds to equation (10) in SH98 and  $B_{z,\text{IMF}}$  and  $p_{\text{dyn}}$  are taken as the mean values in an event-preceding 8-minute interval from the solar wind OMNI dataset, taking the time delay from the bow shock to the magnetopause and the terminator into account. With definition (4), a negative  $\Delta R_0$  corresponds to a compression and a positive  $\Delta R_0$  to an expansion of the magnetopause to the spacecraft location.

We decided to project each of the observed MP location to its equivalent stand-off distance  $R_0$ . Otherwise, the flank MPCs could lead to a statistical bias towards higher values for MP position and model deviation, since the flank MP is naturally farther away from Earth and moves with higher amplitudes compared to the subsolar MP. We acknowledge that our method introduces errors associated with real flaring parameter differences to the SH98 model, which we discuss later in more detail.

In some cases ( $\sim 11\%$ ) the stand-off distance and the deviation could not be calculated due to a lack of OMNI data for an entire interval, we have excluded the corresponding MPC entries from our database.

For each found MPC, we infer a crossing probability from the prediction probability  $p_{\text{RF}}(t)$  given by the RF classifier. The calculation is a weighted average of the probability of the 2 points before and after the jump in the labels:

$$p_{\text{MPC}}(t_0) = \frac{1}{3} [p_{\text{RF}}(t_0 - 12 \text{ s}) + 0.5p_{\text{RF}}(t_0) + 0.5p_{\text{RF}}(t_0 + 12 \text{ s}) + p_{\text{RF}}(t_0 + 24 \text{ s})]. \quad (6)$$

The points are weighted with increasing time distance from the jump with 0.5 or 1 (see (6)), as the RF classifier predicts the labels with higher precision further away from the jump. The two points directly adjacent to the label change have the biggest prediction uncertainty and should contribute less to the probability calculation.

MPCs with low crossing probability are more likely misidentified or ambiguous. Thus, it is reasonable from here on to only use the roughly 75% of the database with high ( $> 0.75$ ) crossing probabilities (121,770 MPCs of TH-MPC). Additionally, as can be seen in Fig. 5, the MPC distributions with and without low crossing probability deviate essentially in count of events.

We point out that some misidentified crossings may still be left in the database, particularly in the high longitude region near the terminator, where a clean identification of crossings can be difficult, due to KHI-induced plasma mixing. Other misidentified crossings, which are still included in the database, are multiple crossings associated to a single extended magnetopause adjacent Low Latitude Boundary Layer (LLBL). This layer contains a mixture of magnetospheric and magnetosheath plasmas (e.g., Hasegawa, 2012), making a clear separation of the regions difficult and false multiple crossing detections more likely.

#### 4 Magnetopause Crossing Statistics

Fig. 5 displays the distribution of all identified MPCs in the database over the stand-off distance, the deviation from the SH98 model in that distance and the latitude and longitude angles of the crossing positions. Separate distributions are shown for higher ( $> 0.75$ ) and lower ( $< 0.75$ ) crossing probabilities. In the top panel (a), the stand-off distance distribution is shown. We see a clear asymmetry around the maximum which lies roughly between  $10.5$  and  $11 R_E$ : At  $11.5 R_E$  a sharp decrease is seen, while for the smaller  $R_0$  we see a smooth slope. The  $\Delta R_0$  distribution (panel (b)) indicates a tendency of the SH98 model to predict the MP a little nearer to Earth, as the maximum is at about  $0.25 R_E$ . This may result from the fact that Shue et al. (1997, 1998) only used the innermost MPCs for fitting their model, while we do not restrict the database. Most of the MPCs are found between  $-1$  and  $1 R_E$  ( $\sim 80\%$ ) which is consistent with reported SH98 model accuracies of  $\sim \pm 1 R_E$  (Case & Wild, 2013; Staples et al., 2020). As can be seen in the bottom two panels (c) and (d), the THEMIS orbits lead to MPC observations (1) being widely distributed in longitude ( $|\lambda| < 90$ ) over the dayside and (2) being restricted in latitude to the near-equatorial region ( $|\theta| < 30$ ).

If we compare the  $R_0$ -distribution with the distribution of the five THEMIS spacecraft dwell times at specific locations (Fig. 6), we see that the probes spent much more time in regions with  $R_0 < 11 R_E$ . Thus, the asymmetry in the MPC distribution results from this orbit bias which naturally leads to more MPCs at smaller stand-off distances. To compensate this orbit bias, we normalize the distributions, dividing the MPC count by the corresponding cumulative dwell time of all THEMIS spacecraft in each bin.

The normalization results can be seen in Fig. 7 showing the probability distribution of MPCs per hour of spacecraft observation time and also a comparison between

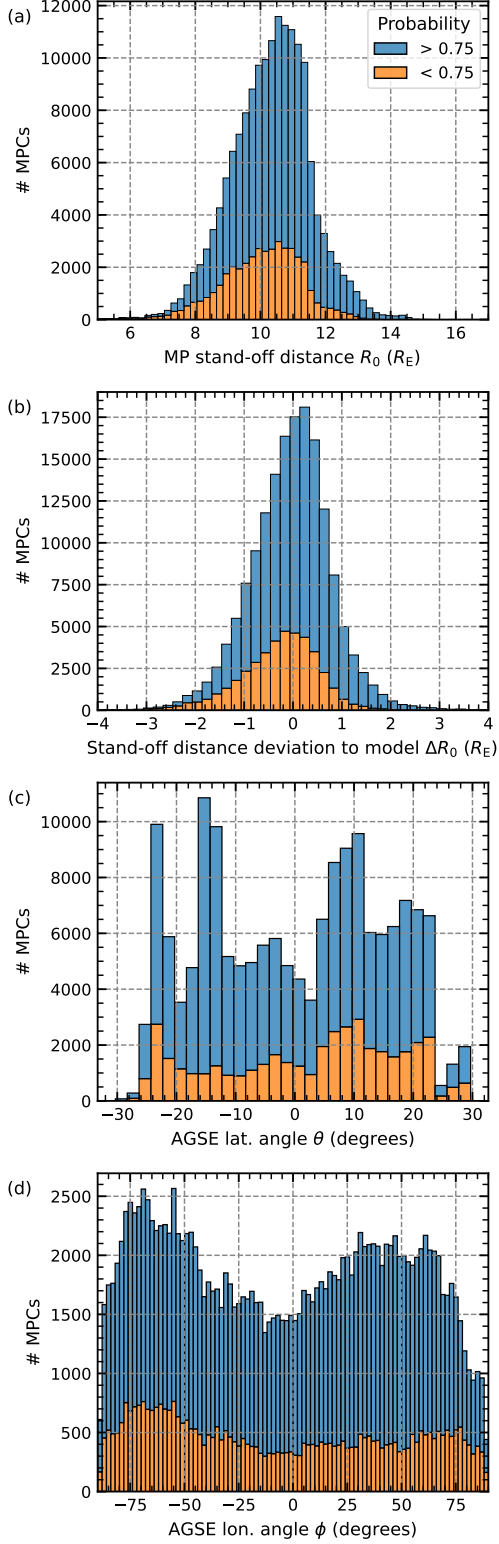


**Figure 5.** Distribution of detected MPCs, with detection probability  $\leq 0.75$  in blue and  $> 0.75$  in orange. The panels show from top to bottom the stand-off distance of the MP, the deviation of this distance from the SH98 model stand-off distance, the latitude angle and the longitude angle of the respective MPCs in AGSE coordinates.

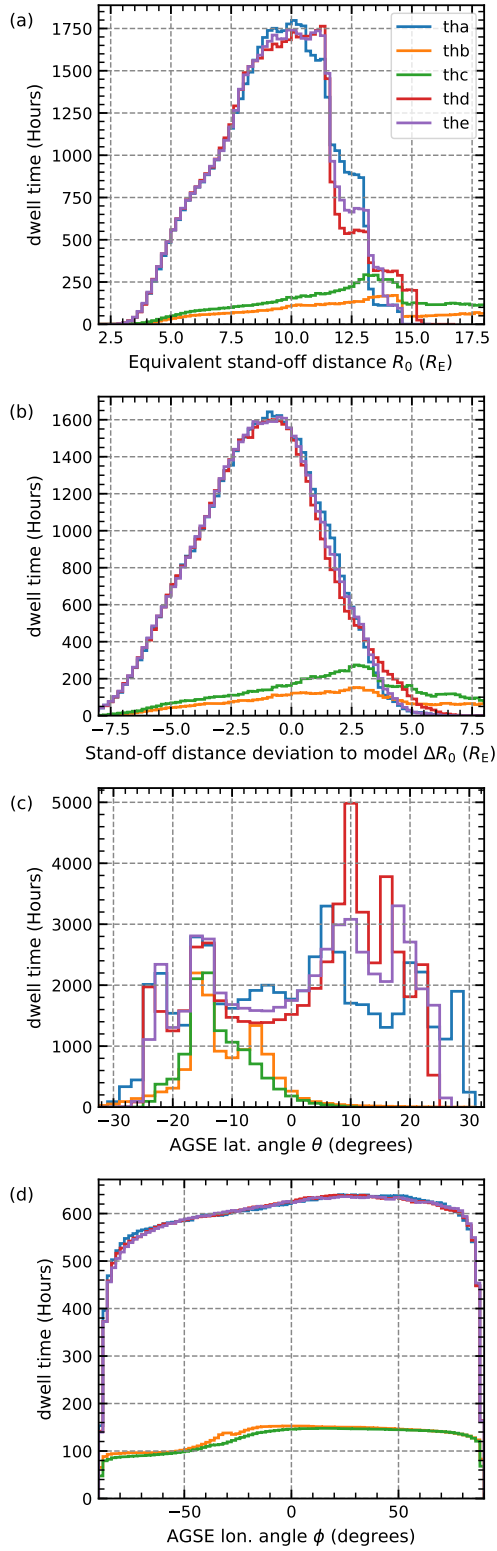


**Figure 6.** Dwell time distributions of the five THEMIS spacecraft with respect to the stand-off distance of the MP, the deviation of this distance from the SH98 model stand-off distance, the latitude angle and the longitude angle in AGSE coordinates (top to bottom).

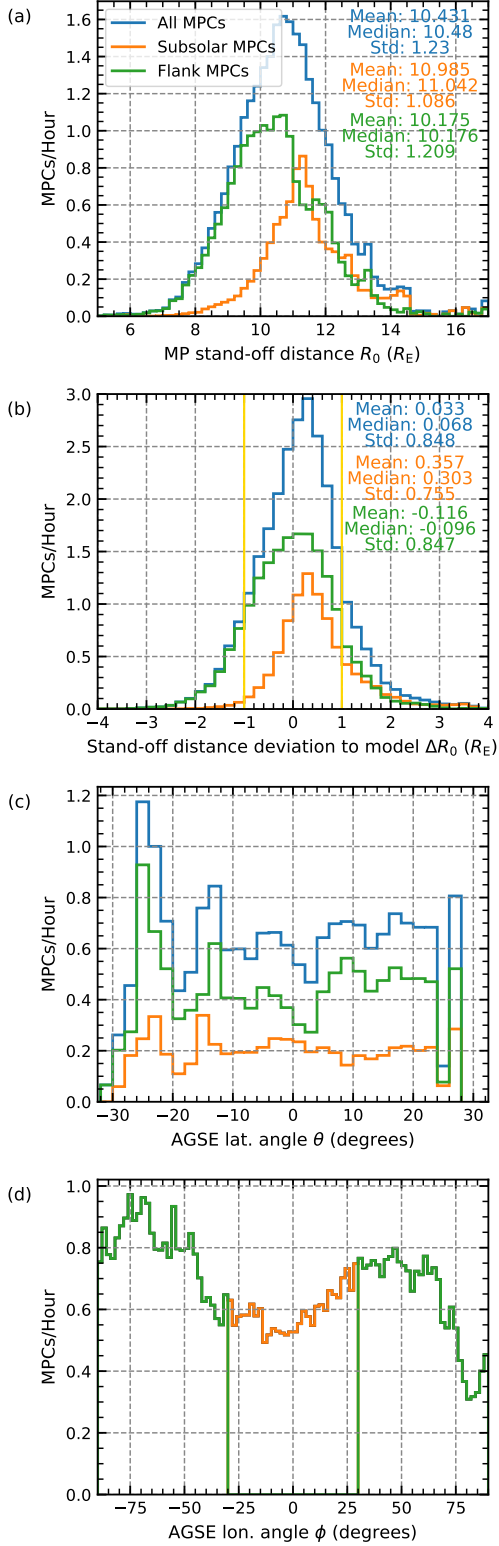


**Figure 7.** Histograms of the normalized distributions, showing crossing events per hour for each bin. The panels show the same variables as Fig. 3. The blue histogram depicts the hole dataset, while the orange and green histograms depicts the subsolar ( $|\lambda| < 30$ ) and the flank ( $|\lambda| > 30$ ) magnetopause subsets, respectively. The yellow line in panel 2 represents the uncertainty of the SH98 model.

448 subsolar ( $|\lambda| \leq 30^\circ$ ) and flank ( $|\lambda| > 30^\circ$ ) MPCs. The orbital bias in the stand-off dis-  
 449 tance (top panel) is no longer visible and the distribution is quasi symmetrical around  
 450  $10.7 R_E$  indicated by the very similar mean and median values of the distribution. In-  
 451 terestingly, the subsolar MPCs occur slightly less frequently (0.86 MPCs/h) and the cor-  
 452 responding distribution is quite narrow in comparison to the broader flank MPCs dis-  
 453 tribution, which is centred around  $10.5 R_E$ .

454 The SH98 model MP is dependent on the flaring parameter  $\alpha$  and the stand-off dis-  
 455 tance  $R_0$ . On the day side, the flaring parameter has little influence on the MP position.  
 456 Thus, adapting the SH98 MP to the MPC observations is achieved by changing the stand-  
 457 off distance. At the flanks, motion of the MP results in variability of  $\alpha$ . Since we fix the  
 458 value of  $\alpha$  with the prevalent solar wind conditions, all MP motion is attributed to changes  
 459 in  $R_0$ , potentially leading to a broader distribution in this parameter (see Fig. 7a).

460 In the distribution of the deviations to the model (Fig. 7, panel (b)), the tendency  
 461 to observe MPCs further away from Earth in comparison to model predictions is visi-  
 462 ble. Significant positive deviations from the SH98 model ( $\Delta R_0 > 1$ ) result from expan-  
 463 sions of the MP in the subsolar and flank regions while the significant negative devia-  
 464 tions ( $\Delta R_0 < -1$ ) result almost only from MP compressions in the flank regions.

465 Looking at the angular distributions of the MPCs, we find a notable asymmetry  
 466 between the dawn and dusk sectors in the longitude distribution (bottom panel). The  
 467 mean occurrence rate between  $-90^\circ$  and  $-30^\circ$  (dawn) is 0.79 MPCs/h while the rate be-  
 468 tween  $30^\circ$  and  $90^\circ$  (dusk) is 0.63 MPCs/h. In the subsolar sector the occurrence is in  
 469 general lower than at the flank sectors (0.59 MPCs/h).

470 The MPCs are more or less equally distributed in latitude (panel (c)).

## 471 5 Solar Wind Statistics

### 472 5.1 Data Selection

473 The SH98 model magnetopause's location and shape are solely influenced by the  
 474 solar wind dynamic pressure  $p_{\text{dyn}}$  and the IMF  $B_z$ -component. The model is nominally  
 475 suitable to make predictions under extreme solar wind conditions which can lead to large  
 476 deformations of the magnetopause (Shue et al., 1998). However, as shown in panel (b)  
 477 of Fig. 7, we find numerous MPCs ( $\sim 20\%$ ) outside the model uncertainties of  $\pm 1 R_E$  oc-  
 478 ccurring with rates  $\leq 1.0$  MPCs per hour.

479 About 7% of the MPCs in the database are classified as extreme deviations from  
 480 the model stand-off distances, surpassing  $\pm 1.5 R_E$ . Positive deviations correspond to mag-  
 481 netospheric expansions and negative deviations to magnetospheric compressions, in the  
 482 following called expanded MPCs and compressed MPCs, respectively. From Fig. 7 we  
 483 can infer that extreme expansions occur with rates  $\leq 0.57$  MPCs per hour and extreme  
 484 compressions with rates  $\leq 0.38$  MPCs per hour.

485 These considerably deviating MPCs may be influenced by solar wind parameters  
 486 that are not considered in the SH98 model. For this study, we associate each MPC from  
 487 the high probability TH-MPC database with one set of solar wind parameters, comprised  
 488 of the medians of the IMF magnitude  $B_{\text{IMF}}$ , the cone angle  $\vartheta_{\text{cone}}$  between the Earth-Sun-  
 489 line and the IMF vector, the clock angle  $\vartheta_{\text{clock}}$  between the IMF  $B_y$ - and  $B_z$ -components,  
 490 the solar wind velocity  $u_{\text{sw}}$ , the ion density  $n_{\text{ion}}$ , the ion temperature  $T_{\text{ion}}$ , the dynamic  
 491 pressure  $p_{\text{dyn}}$ , the plasma  $\beta$  and the Alfvénic Mach number  $M_A$ , based on OMNI mea-  
 492 surements form 8-minute intervals preceding each MPC.

493

## 5.2 Parameter Influence

494

495

496

497

498

To quantify the contribution of different solar wind parameters to the magnetopause distortions, we compare the whole distribution of the solar wind parameters from our OMNI dataset with the solar wind parameters associated with the TH-MPC database and the two extreme MPC subsets of expanded MPCs and compressed MPCs. We normalize each distribution individually by the total number of contributing data points.

499

500

501

502

503

The distributions with respect to  $B_{\text{IMF}}$ ,  $\vartheta_{\text{cone}}$ ,  $\vartheta_{\text{clock}}$ ,  $u_{\text{sw}}$ ,  $n_{\text{ion}}$ ,  $T_{\text{ion}}$ ,  $p_{\text{dyn}}$ , plasma  $\beta$  and  $M_A$  are shown in Figure 8. The OMNI data are shown in black and serves as reference. The solar wind data during the MPCs are shown in blue, while the orange and green lines display the distributions associated with extreme MPCs. The maxima and medians of the datasets are displayed as well, equally colour coded.

504

505

506

507

508

509

510

511

512

513

514

515

516

517

518

519

The solar wind data distributions (in black) agree nicely with results from previous studies (e.g., Plaschke et al., 2013; L. Q. Zhang et al., 2019; Larrodera & Cid, 2020; Ma et al., 2020). Furthermore, for all parameters we find an expected similarity in shape and maximum values between the blue and black distributions, as MPCs should be observed under all possible solar wind conditions over the long time range considered in this study. However, some of the distributions associated with extreme MPCs notably differ from the reference distributions, particularly with respect to  $\vartheta_{\text{cone}}$ ,  $u_{\text{sw}}$ ,  $T_{\text{ion}}$  and  $M_A$ , indicating an influence of these parameters on the occurrence of extreme MP distortions. We compute the quotient of the distributions corresponding to the extreme MPCs with the reference solar wind distributions to indicate favourable occurrence conditions in the solar wind parameters. These favourable conditions are visible in quotient maxima above 1 and unfavourable conditions in minima under 1. In Fig. 9 these deviations from the reference distributions are displayed. The errors are computed using the mean detection rate of 15 MPCs per 1-hour interval as typical count error. In the following, we discuss the solar wind parameter distributions in the order of ascending influence on the extreme MPCs.

520

521

522

523

524

525

526

527

528

529

All clock angle distributions (Fig. 8F) show a double peak structure representing the known feature of the Parker spiral (e.g., L. Q. Zhang et al., 2019). In addition, we see small deviations in shape with respect to the reference solar wind distribution over all angles. Some clock angle orientations appear to be slightly more beneficial for the occurrence of extreme MPCs (see Fig. 9F). For example, the compressed MPCs show a tendency to occur under southward IMF conditions ( $|\vartheta_{\text{clock}}| \geq 100^\circ$ ) and the distribution for the expanded MPCs deviates noticeable around  $0^\circ$ , corresponding to occurrences during northward IMF. However, the positive deviations from 1, which can indicate favourable conditions seen in Fig. 9F are rather small in comparison to deviations in other parameters.

530

531

532

533

534

535

536

537

538

Although, the influence of the dynamic pressure on the magnetopause location should be captured by the SH98 model, we still see some subtle deviations in the distributions (panel J in Fig. 8) hinting at a further influence. We ignore the high peak at 0.3 nPa for the compressed MPCs in Fig. 9J as this large deviation results from only very few MPCs in this bin. Favourable conditions for extreme compressed MPCs are slightly higher pressures between 1.8 nPa and 3.5 nPa. The extreme expanded MPCs occur preferably under weaker pressures around 1.1 nPa. In both cases, however, the deviations in the distribution quotients found are less than 1.5. We conclude that the effect of dynamic pressure on extreme MPCs is already well captured by the SH98 model, as expected.

539

540

541

542

The distributions of plasma  $\beta$  (Fig. 8K) for extreme MPCs are slightly shifted with respect to the reference distribution. This shift is clearly visible in the maximum and the median values of the distributions. From Fig. 9K we infer that MP expansions occur more frequently for slightly higher  $\beta$  values between 2 and 5, and compressions are

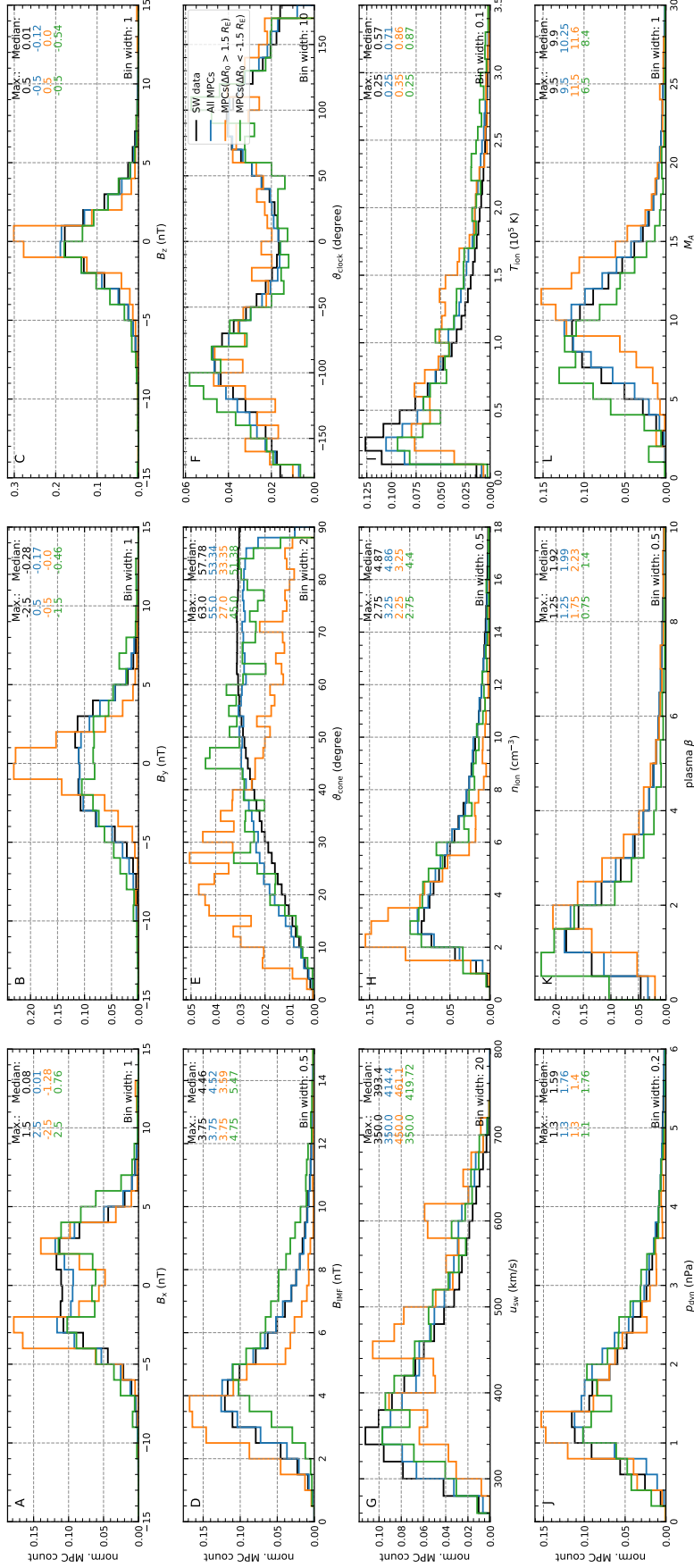


**Figure 8.** Probability distributions of different solar wind parameters. In each panel the whole solar wind distribution of a specific parameter (black lines) is compared to the parameter distribution pertaining to all MPCs (blue lines) and the extreme MPCs (orange and green lines, respectively). The maximum and the median values are indicated in each panel. All distributions are normalized by the total number of contributing data points.

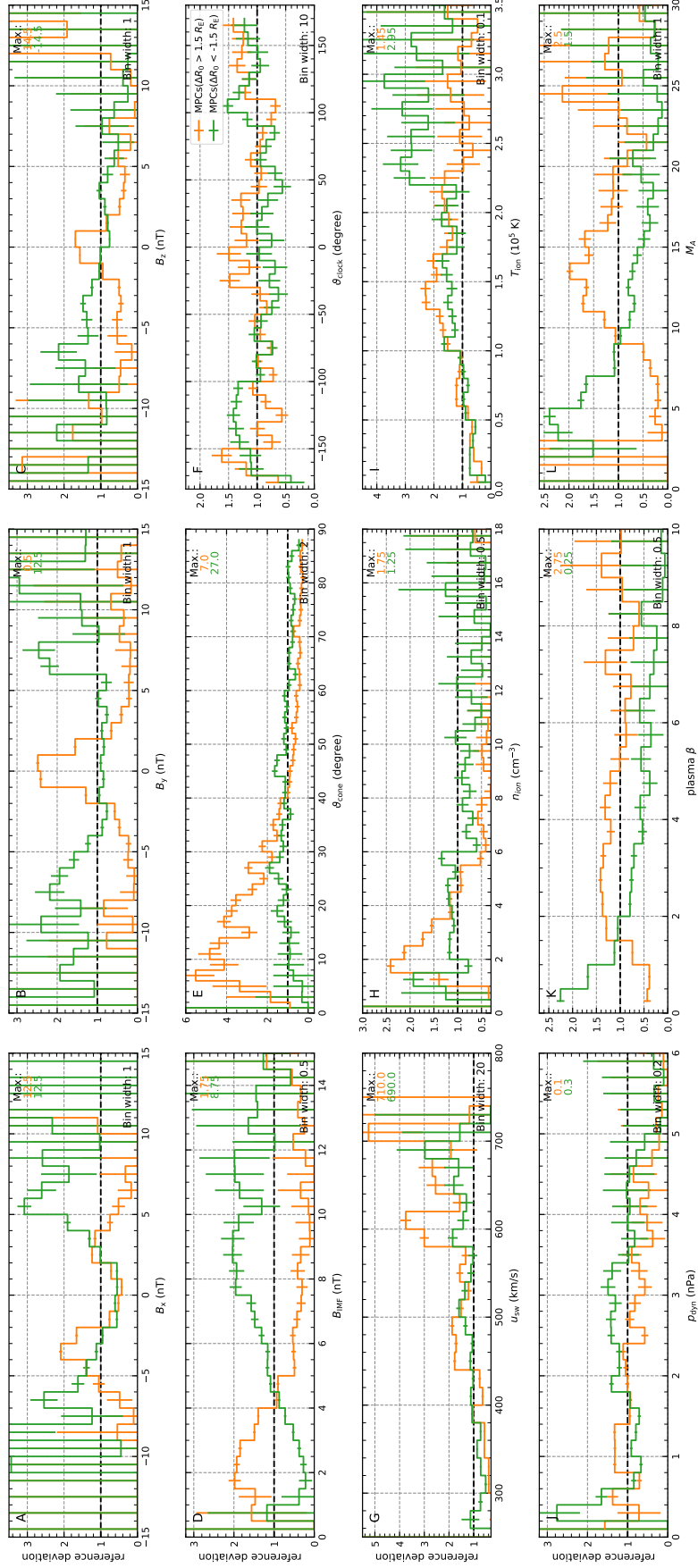


**Figure 9.** Deviations from the reference distributions (see Fig. 8) corresponding to extreme MPCs, calculated by dividing the distribution by the reference. The orange lines correspond to expanded MPCs and the green lines correspond to compressed MPCs.

543 more frequent for lower values below 1. Thus, higher/lower values lead to more frequent  
 544 expansions/compressions.

545 In the ion density distributions (Fig. 8H), we find quite different deviations of the  
 546 distributions for expanded and compressed MPCs. For the expanded MPCs, we can infer  
 547 from Fig. 9H a clear tendency of higher occurrence rates between density values of  
 548  $1.5 \text{ cm}^{-3}$  and  $3.5 \text{ cm}^{-3}$ . For the compressed MPCs, we find one peak at  $n_{\text{ion}} = 1.25$   
 549  $\text{cm}^{-3}$  which might be not reliable, as the bin contains only few MPCs. The other positive  
 550 deviation for density values between  $2 \text{ cm}^{-3}$  and  $6 \text{ cm}^{-3}$  in the distribution quotient  
 551 is very small.

552 Interestingly, all temperature distributions (Fig. 8I) share a common maximum around  
 553  $3 \cdot 10^4 \text{ K}$ , but differ quite a lot in the median values. We find that the distributions for  
 554 extreme MPCs are shifted to higher  $T_{\text{ion}}$ . Both compressed and expanded MPCs seem  
 555 to occur more frequently in the temperature range between  $1.0 \cdot 10^5 \text{ K}$  and  $2.1 \cdot 10^5 \text{ K}$  (see  
 556 Fig. 9I). Higher  $T_{\text{ion}}$  are favourable only for the compressed MPCs. However, in this tem-  
 557 perature range we only observed very few MPCs.

558 From the three IMF components displayed in Fig. 8 and 9A - C we can also infer  
 559 favourable conditions. Expanded MPCs occur more frequently for  $B_x$  around  $\pm 3 \text{ nT}$  (neg-  
 560 ative values occur more often) and  $B_y$  around  $0 \text{ nT}$ . The compressed MPCs occur more  
 561 often under even higher values of  $B_x$  around  $\pm 6 \text{ nT}$  and for  $B_y$  values around  $\pm 7.5 \text{ nT}$ .  
 562 The influence of  $B_z$  is again well captured by the S98 model. However, similar to the  
 563 influence of  $p_{\text{dyn}}$  we see some possible significant deviations regarding the compressed  
 564 MPCs for strong negative values hinting at a favourable condition for these with  $B_z$  be-  
 565 tween  $-5$  and  $-9 \text{ nT}$ .

566 In panel D of Fig. 8 and 9 we can see that extreme expanded MPCs occur more  
 567 frequently for smaller IMF magnitudes, with  $B_{\text{IMF}}$  between  $1.5 \text{ nT}$  and  $4 \text{ nT}$ . In con-  
 568 trast, the distribution of the extreme compressed MPCs is shifted to higher IMF mag-  
 569 nitudes, indicating favourable conditions above  $6 \text{ nT}$ .

570 Fig. 8L, depicting the Alfvén Mach number distributions, shows obvious deviations  
 571 between the reference and the extreme MPC distributions. The maxima and medians  
 572 for the compressed and expanded MPCs deviate substantially from the reference, and  
 573 we can clearly infer favourable conditions from Fig. 9L: For the expanded MPCs, we see  
 574 the maximal occurrence rate at  $M_A = 11.5$  and favourable conditions of  $M_A$  between  
 575  $11$  and  $16$ . For the compressed MPCs, we find the maximum at  $M_A = 4.5$  and favourable  
 576 conditions of  $M_A$  between  $3$  and  $7$ .

577 Both expanded and compressed MPCs seem to occur more frequently under high  
 578  $u_{\text{sw}}$  conditions (above  $440 \text{ km/s}$ ). This trend is more clearly visible for the expanded MPCs  
 579 (see Fig. 8G and 9G).

580 Lastly, we find a significant influence of  $\vartheta_{\text{cone}}$  on extreme expanded MPCs. Quasi-  
 581 radial IMF conditions ( $\vartheta_{\text{cone}} < 35^\circ$ ) clearly favour expanded MPCs (see panel E in Fig.  
 582 8 and 9). No similar feature can be seen with respect to the occurrence of compressed  
 583 MPCs as a function of  $\vartheta_{\text{cone}}$ . However,  $\vartheta_{\text{cone}} 25^\circ$  and  $30^\circ$  could be a favourable condi-  
 584 tion for the compressed MPCs.

## 585 6 Discussion

586 In Fig. 7 (a), we find a quite symmetrical distribution of stand-off distances around  
 587  $10.7 R_E$ , which can be regarded as typical (e.g. Baumjohann & Treumann, 1997). In com-  
 588 parison with stand-off distance predictions by the Shue et al. (1998) model (panel (b)),  
 589 we find a slight tendency of the model to underestimate the stand-off distance, which

590 probably results from the fact that Shue et al. (1998) only used the innermost crossings  
591 of MP encounters for fitting the model parameters.

592 In the longitude distribution of the MPCs (panel (d) of Fig. 7) we see a tendency  
593 to observe more MPCs at the magnetospheric flanks and a clear asymmetry between the  
594 occurrence rates in the dawn and dusk sectors. At the flanks, occurrences of KHI waves  
595 are likely (Taylor et al., 2012; Johnson et al., 2014) which should lead to frequent move-  
596 ment of the MP and more observations of MPCs. Additionally, as already mentioned,  
597 the Random Forest machine learning algorithm has some difficulties to clearly distinguish  
598 the magnetosphere and magnetosheath regions in case of thicker boundary layers lead-  
599 ing to multiple crossing detections. We try to mitigate this problem by only studying  
600 MPCs with high crossing probabilities. Some remnants of this multiple MPCs might still  
601 be in the database, resulting in a tendency to observe more flank MPCs.

602 The dawn-dusk asymmetry is unlikely to be due to an orbital observation bias, as  
603 we have removed the bias corresponding to the spacecraft orbit using the spacecraft dwell  
604 time. Furthermore, our database is extensive enough that there should be no significant  
605 differences in the solar wind conditions prevalent during dawn and dusk MPCs. A dawn-  
606 dusk asymmetry in MPC occurrences has also been previously reported for the MPCs  
607 in the tail of the magnetosphere (e.g., Howe & Siscoe, 1972), and we can find the asym-  
608 metry in previous studies of the dayside MP. For example, Staples et al. (2020) used a  
609 threshold-based detection algorithm to study MPCs observed by THEMIS. Their MPC  
610 distributions (see Fig. A1) and ours are very similar, giving us confidence in our detec-  
611 tion method using the Random Forest Classifier.

612 For Parker Spiral orientated IMF, KHIs predominately occur on the dawn flank  
613 (Henry et al., 2017), which might explain the previous statistical results. However other  
614 studies (e.g. Taylor et al., 2012) report on more frequent KHI occurrences at the dusk  
615 flank. Thus, KHIs might not be solely responsible for our observed slightly higher oc-  
616 currence rate for MPCs at the dawn flank of the magnetosphere. Walsh et al. (2014) pointed  
617 out that the dawn flank has a thicker magnetopause boundary layer, which may give more  
618 weight to a possible explanation in terms of multiple MPC detections by the Random  
619 Forest Classifier. Another explanation for the asymmetry could be that the magnetopause  
620 moves more frequently in the dawn sector due to the thinner and more turbulent mag-  
621 netosheath (Walsh et al., 2014). The foreshock will more often be located in this sector  
622 and excite more frequent MP movement, resulting in more frequent MPCs and there-  
623 fore in higher occurrence rates. This foreshock effect on MP motion is also discussed in  
624 Russell et al. (1997) and is most likely related to the pressure variations associated with  
625 the foreshock region.

626 By comparing our database to the mentioned Staple et al. (2020) database, we can  
627 find out which explanation might be more reasonable. They looked at THEMIS data from  
628 2007 to 2016 and only kept the innermost crossings of multiple MPCs in a 10-min in-  
629 terval. With the removal of multiple crossings, the above-mentioned higher occurrence  
630 rates due to KHIs or the detection method should not be visible in the distributions from  
631 Staples et al. (2020). However, as mentioned before, their database is subject to the dawn-  
632 dusk asymmetry in MPC occurrences. Hence, the reason for this asymmetry is more likely  
633 the more frequent occurrence of MP movement in the dawn sector possible linked to the  
634 foreshock or the more turbulent magnetosheath downstream of the quasi-parallel shock.  
635 Nevertheless, further investigations are necessary to fully understand this dawn-dusk asym-  
636 metry in MPC occurrences.

637 The statistical analysis above of the whole MPCs database is rather limited. Other  
638 studies like, e.g., Nguyen et al. (2022b) looked in more detail on the overall response of  
639 the magnetosphere to different solar wind parameters. Since we want to focus on the ori-  
640 gin of the unusual MP locations, we only use the overall statistics to validate our iden-  
641 tification method by comparing our results with those of previous studies. In doing so,

642 we can see that some of our statistics regarding the whole MPC database (blue distri-  
 643 butions in Fig. 8) are very similar to those found by Nguyen et al. (2022b). However,  
 644 our statistical analysis revealed a clear asymmetry between the occurrence of MPC on  
 645 the dawn and dusk flanks, which has not been clearly shown in other studies. In addi-  
 646 tion, we point out the influence of solar wind parameters on the occurrence of extreme  
 647 MPCs. This is something that has rarely been discussed.

648 Let us now have a look at the roughly 7% of the identified MPCs that deviate dras-  
 649 tically from the model predictions, that may not be immediately explained by changes  
 650 in the solar wind dynamic pressure or the  $B_z$ -component of the IMF. From the compar-  
 651 ison of the solar wind parameters during these extreme MPCs with the standard solar  
 652 wind parameter distributions, we are able to infer some significant solar wind param-  
 653 eter influences on magnetopause location:

654 The most obvious influence pertains to the IMF cone angle, which controls the ex-  
 655 pansion of the magnetosphere as reported before (e.g., Slavin et al., 1996; Merka et al.,  
 656 2003; Suvorova et al., 2010; Park et al., 2016; M. Wang et al., 2020). Under radial or quasi-  
 657 radial IMF conditions, the dayside bow shock location is closer to Earth than on aver-  
 658 age, the magnetosheath thickness decreases, and the dayside magnetopause moves sun-  
 659 ward. This happens in parts due to the establishment of a quasi-parallel foreshock in the  
 660 subsolar region, which redistributes the dynamic pressure of the solar wind plasma and  
 661 yields a lower magnetic pressure, affecting the magnetosphere. Additionally, the total  
 662 plasma pressure is strongly modified in the bow shock crossing and distributed due to  
 663 the flow diversion in the magnetosheath across the dayside magnetopause surface (Suvorova  
 664 et al., 2010; Samsonov et al., 2012) leading to an expanding magnetopause to re-establish  
 665 the pressure balance.

666 Extreme compressions might also occur under quasi-radial IMF conditions ( $\vartheta_{\text{cone}} \approx$   
 667  $30^\circ$ ). As Archer and Horbury (2013), Plaschke et al. (2013) and LaMoury et al. (2021)  
 668 point out, HSJs occur more often under these conditions. Shue et al. (2009) and Archer  
 669 et al. (2019) observed significant indentations of the magnetopause caused by a HSJ un-  
 670 der radial IMF. Thus, the higher occurrence rate for compressions may be linked with  
 671 such HSJs. However, the scale sizes of HSJ are small (Plaschke et al., 2020) leading only  
 672 to a local indentation of the MP. Thus, its much more likely that the MP response to the  
 673 radial IMF on global scale is an expansion of the MP. This is also suggested by the dis-  
 674 tributions in Fig.9E, as the deviations for the expanded MPCs are clearly more signif-  
 675 icant in our database.

676 Substantial influences on extreme MP distortions stemming from the magnitude  
 677 of the IMF, the plasma  $\beta$  and the Alfvén Mach number might in fact result from the same  
 678 source: Extreme expansions of the magnetopause occur more frequently for small IMF  
 679 magnitudes, i.e., values like the Alfvén velocity or the magnetic pressure are small as well.  
 680 Naturally, small magnetic pressures and Alfvén velocities lead to higher plasma  $\beta$  and  
 681 Alfvén Mach numbers, respectively, which are favourable conditions for extreme mag-  
 682 netospheric expansions as well. The expansions are possibly related to the higher par-  
 683 ticle reflection rates, leading to stronger kinetic energy dissipation at the bow shock un-  
 684 der these condition (Winterhalter & Kivelson, 1988; Treumann, 2009), strengthening the  
 685 foreshock region and thereby reducing the pressure on the dayside magnetosphere. On  
 686 the contrary, the compressed MPCs occur more frequently for low Mach numbers and  
 687 low plasma  $\beta$ , which result from higher IMF magnitudes. This might be connected to  
 688 the fact, that the solar wind Mach number controls the magnetosheath plasma  $\beta$ . For  
 689 low magnetosheath plasma  $\beta$  resulting from low solar wind Mach numbers, reconnection  
 690 is more likely, leading to flux erosion and compression of the magnetosphere. Further-  
 691 more, we can infer that for magnetospheric compressions the magnetic pressure is dom-  
 692 inant in the solar wind ( $\beta < 1$ ), and for the magnetospheric expansions thermal pres-  
 693 sure is dominant ( $\beta > 1$ ).

Both in the velocity and in the temperature distributions (Fig. 8G and I), we identified a shift to higher values for extreme MPCs, especially noticeable for magnetospheric expansions. These higher values in the velocity probably lead to an increase in the velocity shear across the magnetopause triggering stronger KHIs and subsequently exciting extreme oscillatory MP motion (Kavosi & Raeder, 2015). Additionally, Chu et al. (2017) and Vu et al. (2022) found that many different foreshock structures like FBs and HFAs were observed during radial IMF with solar wind velocities around 600 km/s. Generally, the favourable conditions of fast solar wind with large Alfvén Mach numbers and low cone angles for the extreme expansions coincide with favourable conditions for the occurrence of these foreshock transients (H. Zhang et al., 2022). These phenomena are characterized by hot tenuous plasma regions in the foreshock region, in which flow deflection and pressure reduction occur (Turner et al., 2013). On impact on the MP this pressure "hole" lead to an expansion followed by a compression of the magnetosphere (e.g., Sibeck et al., 1999; Turner et al., 2011; Archer et al., 2014, 2015). Thus, these foreshock transients might play an additional role in the extreme expansions and compressions of the magnetopause.

The  $B_x$  and  $B_y$  components of the IMF also seem to have major influences on the occurrence of extreme MPCs. Higher occurrence rates for expanded MPCs with  $B_y=0$  and  $B_x$  strongly anti-sunwards indicate again a quasi-radial IMF as favourable conditions for such events. Therefore, the major deviations in the cone angle distribution might solely stem from the  $B_x$  influence. Results from simulations (Lu et al., 2013) suggest that for increasing IMF  $B_y$  the MP moves earthwards. This might be an important effect, as compressed MPCs occur more often for higher  $B_y$  values.

Weak but noticeable deviations in the clock angle distributions may stem from residual effects of the IMF  $B_z$  component, which is captured in the SH98 model. The possible favourable condition around  $0^\circ$  for expanded MPCs coincide with fact that the magnetopause stand-off distance is larger for northward IMF, when no reconnection and flux erosion is happening at the dayside. For southward IMF reconnection and flux erosion occur, driving the MP inwards and favouring observations of compressed MPCs under this condition.

The influence of the dynamic pressure is already prominently captured in the SH98 model. Therefore, the pressure effect would not appear as substantial deviation in our plots. As expected, similar behaviours can be found for the  $B_z$  component.

The deviation in the density distributions (Fig. 9H) for the compressed MPCs are also negligible, showing no significant favourable condition. In the distribution associated with the expanded MPCs we can see a minor preference for more tenuous solar wind plasma. Tenuous plasma causes a decrease in the thermal pressure, therefore reducing the total pressure impacting the magnetosphere.

Overall, we find more significant deviations from the reference distributions associated with the expanded MPCs, i.e., magnetospheric expansions are less well covered by the SH98 model. Therefore, we identify more favourable conditions for a extreme magnetospheric expansions. All influences on the magnetosphere presented here are additional effects besides the effects captured in the SH98 model. Not all of the effects might be solely responsible for the visible deviations in the distributions. To figure out which effects are most likely, further investigations are needed.

It should be emphasised that we use the SH98 model to identify extreme events deviating from the model. This model uses only two parameters for its prediction of the MP location and may miss previously reported influences on the MP stemming from the dipole tilt or other IMF components (Lin et al., 2010; Liu et al., 2012; Lu et al., 2013). However, the SH98 model is widely used in the community and is able to predict the equatorial MP well on average. Therefore, we choose to use this model over others because

of its simplicity. Of course, this could lead to a misinterpretation of our results, as the observed deviations could be due to the influence of the dipole tilt. To ensure that dipole tilt did not influence our results, we looked for seasonal effects in our distributions. Although we were able to find some variations between the winter and summer periods, there is no significant systematic influence of the dipole tilt on our results. This was expected, as Lu et al. (2013) indicated that dipole tilt does not affect the variation of equatorial MP.

## 7 Conclusion

In this study, the last 15 years of THEMIS observations have been used to build a very large MPC database. This database allows us to examine extreme MP distortions in detail in special case or statistical studies.

Our statistical study shows that parameters such as the Alfvén Mach number, the IMF cone angle and the ion velocity are responsible for quite frequent occurrences of extreme magnetopause distortions. Quasi-radial IMF conditions with a plasma  $\beta > 1$ , higher Alfvén Mach numbers and ion velocities above 450 km/s are favourable for magnetospheric expansions beyond the SH98 model predictions, while magnetospheric compressions are associated with more southward IMF conditions with plasma  $\beta < 1$ , lower Alfvén Mach numbers and IMF strengths above 5 nT.

The expansions of the magnetopause under high Mach number and velocity conditions are possible linked to KHIs and also foreshock transients, while other phenomena like magnetosheath jets might be responsible for some compressions. This could be studied further by comparing the observation times of such phenomena with our database. In sorting the extreme MPCs by possible origin mechanisms, we also hope to learn more about main drivers behind the extreme events.

Here we only study MPCs in low latitudes, observed on the dayside. With the utilization of CLUSTER data, we plan to expand our database to high latitudes (e.g., Panov et al., 2008), allowing for a comparison between the equatorial and more polar regions.

As some favourable conditions might stem from the same origin, it is also necessary to see if the favourable conditions are distinct from each other or more tightly connected. We plan to do this in a follow-up study.

With the upcoming SMILE mission, the shape and location of the MP will be directly inferred and linked to in-situ measurements of solar wind conditions. This will allow an immediate comparison with the results of this study and open the door for further investigations of extreme MP distortions.

## Appendix A Threshold based MPC database

Staples et al. (2020) used the following criteria for the identification of MPCs on the dayside magnetosphere:

1. During a THEMIS crossing from the magnetosphere to the magnetosheath  $\Delta B_{z,\text{gsm}} < -0.6 \frac{\text{nT}}{\text{s}}$  and  $\Delta n_{\text{ion}} > 0.08 \frac{1}{\text{cm}^3 \text{s}}$  should hold over the crossing. These criteria are reversed for crossings from the magnetosheath to the magnetosphere.
2. In average,  $B_{z,\text{gsm}} > 5 \text{ nT}$  and  $n_{\text{ion}} < 7 \text{ cm}^{-3}$  should hold for a 48-s interval within the magnetosphere before/after a possible event.
3. These two criteria must be satisfied in a 60-s-interval.

They completed their database with additional crossings identified by Plaschke, Glassmeier, Auster, Angelopoulos, et al. (2009), then removed duplicate crossings and reduced

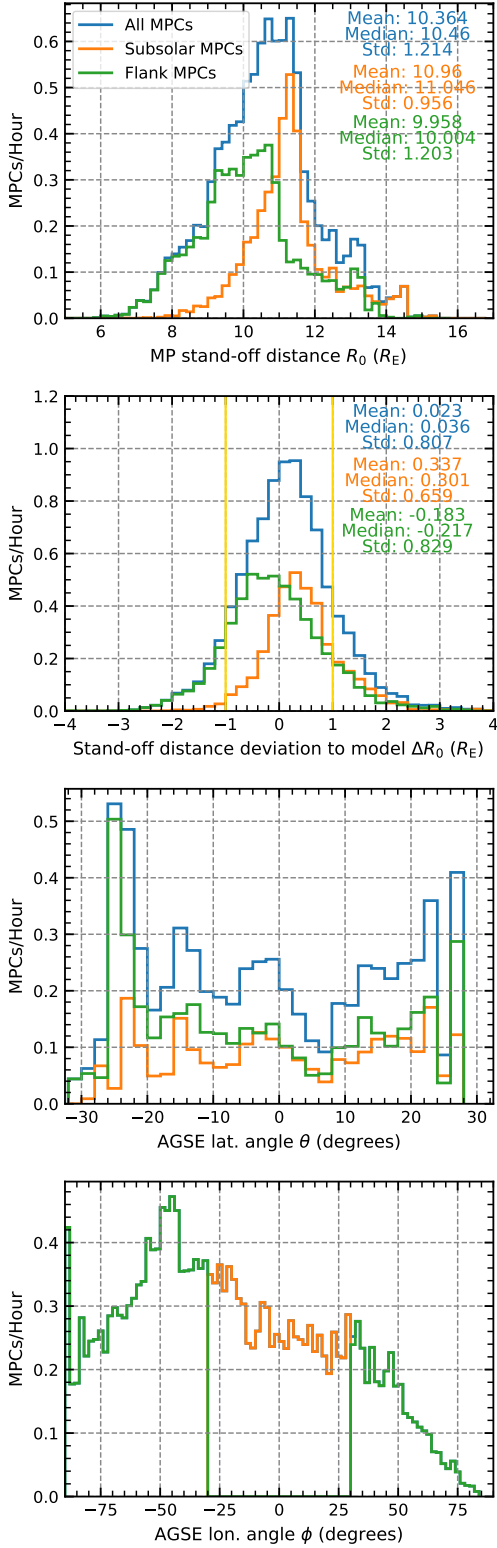


**Figure A1.** Histogram of normalized MPC distribution based on the database by Staples et al. (2020), showing crossing events per hour for each bin. The panels show from top to bottom: The stand-off distance of the MP, the deviation of this distance from the SH98 model stand-off distance, and the latitude and the longitude angles in AGSE coordinates. The blue histogram depicts the hole dataset, while the orange and green histograms depict the subsolar ( $|\lambda| < 30$ ) and the flank ( $|\lambda| > 30$ ) magnetopause subsets, respectively.

790 the database to the innermost crossings. Fig. A1 displays the distributions of their database  
 791 identically normed as our database distributions.

## 792 Open Research

793 The magnetopause crossing event database constructed and used in this study is  
 794 publicly available under <https://osf.io/b6kux/>, hosted by the Open Science Frame-  
 795 work (OSF). To collect and plot data, we used the open source Python Space Physics  
 796 Environment Data Analysis Software (pySPEDAS) which can be found here: [https://](https://github.com/spedas/pyspedas)  
 797 [github.com/spedas/pyspedas](https://github.com/spedas/pyspedas). THEMIS data can be retrieved from <http://themis>  
 798 [.ssl.berkeley.edu/data/themis/](http://themis.ssl.berkeley.edu/data/themis/) and OMNI data from the GSFC/SPDF OMNIWeb  
 799 interface at <https://omniweb.gsfc.nasa.gov>. The machine learning task were performed  
 800 with the scikit-learn Python library, from which we utilized the implementations of the  
 801 different algorithms. The documentation can be found here: [https://scikit-learn.org/](https://scikit-learn.org/stable/supervised_learning.html#supervised-learning)  
 802 [stable/supervised\\_learning.html#supervised-learning](https://scikit-learn.org/stable/supervised_learning.html#supervised-learning).

## 803 Acknowledgments

804 We acknowledge NASA contract NAS5-02099 and V. Angelopoulos for use of data from  
 805 the THEMIS Mission. Specifically: C. W. Carlson and J. P. McFadden for use of ESA  
 806 data and K. H. Glassmeier, U. Auster and W. Baumjohann for the use of FGM data pro-  
 807 vided under the lead of the Technical University of Braunschweig and with financial sup-  
 808 port through the German Ministry for Economy and Technology and the German Cen-  
 809 ter for Aviation and Space (DLR) under contract 50OC 0302. We thank J. King and N.  
 810 Papitashvili of the National Space Science Data Center (NSSDC) in the NASA/GSFC  
 811 for the use of the OMNI 2 database. FP and JZDM are supported by the Deutsches Zen-  
 812 trum für Luft- und Raumfahrt (DLR) under contract 50OC2201. DH was supported by  
 813 the German Ministerium für Wirtschaft und Klimaschutz and the German Zentrum für  
 814 Luft- und Raumfahrt (DLR) under contracts 50QW1501 and 50QW2202. MOA was sup-  
 815 ported by UKRI Stephen Hawking Fellowship EP/T01735X/1. The authors want to thank  
 816 Nick Hatzigeorgiu and Eric Grimes for the ongoing development of PySPEDAS.

## 817 References

- 818 Angelopoulos, V. (2008, apr). The THEMIS Mission. *Space Sci. Rev.*, *141*(1-4), 5-  
 819 34. doi: 10.1007/s11214-008-9336-1
- 820 Angelopoulos, V. (2011, dec). The ARTEMIS Mission. *Space Sci. Rev.*, *165*(1-4), 3-  
 821 25. doi: 10.1007/s11214-010-9687-2
- 822 Archer, M. O., Hietala, H., Hartinger, M. D., Plaschke, F., & Angelopoulos, V.  
 823 (2019, feb). Direct observations of a surface eigenmode of the dayside magne-  
 824 topause. *Nature Communications*, *10*, 615. doi: 10.1038/s41467-018-08134-5
- 825 Archer, M. O., & Horbury, T. S. (2013, feb). Magnetosheath dynamic pressure en-  
 826 hancements: occurrence and typical properties. *Annales Geophysicae*, *31*(2),  
 827 319-331. doi: 10.5194/angeo-31-319-2013
- 828 Archer, M. O., Turner, D. L., Eastwood, J. P., Horbury, T. S., & Schwartz, S. J.  
 829 (2014, oct). The role of pressure gradients in driving sunward magnetosheath  
 830 flows and magnetopause motion. *Journal of Geophysical Research (Space*  
 831 *Physics)*, *119*(10), 8117-8125. doi: 10.1002/2014JA020342
- 832 Archer, M. O., Turner, D. L., Eastwood, J. P., Schwartz, S. J., & Horbury, T. S.  
 833 (2015, feb). Global impacts of a Foreshock Bubble: Magnetosheath, magne-  
 834 topause and ground-based observations. *Planetary and Space Science*, *106*,  
 835 56-66. doi: 10.1016/j.pss.2014.11.026
- 836 Aubry, M. P., Russell, C. T., & Kivelson, M. G. (1970, jan). Inward motion of  
 837 the magnetopause before a substorm. *Journal of Geophysical Research*, *75*(34),  
 838 7018. doi: 10.1029/JA075i034p07018

- 839 Auster, H. U., Glassmeier, K. H., Magnes, W., Aydogar, O., Baumjohann, W.,  
840 Constantinescu, D., ... Wiedemann, M. (2008, dec). The THEMIS Flux-  
841 gate Magnetometer. *Space Sci. Rev.*, *141*(1-4), 235-264. doi: 10.1007/  
842 s11214-008-9365-9
- 843 Baumjohann, W., & Treumann, R. (1997). *Basic Space Plasma Physics*. Imperial  
844 College Press.
- 845 Branduardi-Raymont, G., Wang, C., Escoubet, C., Adamovic, M., Agnolon, D.,  
846 Berthomier, M., ... Zhu, Z. (2018). SMILE definition study report. *European*  
847 *Space Agency, ESA/SCI*, *1*.
- 848 Breiman, L. (2001, jan). Random Forests. *Machine Learning*, *45*, 5-32. doi: 10  
849 .1023/A:1010933404324
- 850 Breiman, L., Friedman, J. H., Olshen, R. A., & Stone, C. S. (1984). *Classification*  
851 *and Regression Trees (1st Edition)*. Chapman & Hall/CRC. doi: 10.1201/  
852 9781315139470
- 853 Breuillard, H., Dupuis, R., Retino, A., Le Contel, O., Amaya, J., & Lapenta, G.  
854 (2020, sep). Automatic classification of plasma regions in near-Earth space  
855 with supervised machine learning: application to Magnetospheric Multi Scale  
856 2016-2019 observation. *Frontiers in Astronomy and Space Sciences*, *7*, 55. doi:  
857 10.3389/fspas.2020.00055
- 858 Burch, J. L., Moore, T. E., Torbert, R. B., & Giles, B. L. (2016, mar). Magneto-  
859 spheric Multiscale Overview and Science Objectives. *Space Sci. Rev.*, *199*(1-4),  
860 5-21. doi: 10.1007/s11214-015-0164-9
- 861 Case, N. A., & Wild, J. A. (2013, oct). The location of the Earth's magne-  
862 topause: A comparison of modeled position and in situ Cluster data. *Jour-*  
863 *nal of Geophysical Research (Space Physics)*, *118*(10), 6127-6135. doi:  
864 10.1002/jgra.50572
- 865 Chao, J. K., Wu, D. J., Lin, C. H., Yang, Y. H., Wang, X. Y., Kessel, M., ... Lep-  
866 ping, R. P. (2002, jan). Models for the Size and Shape of the Earth's Mag-  
867 netopause and Bow Shock. In L.-H. Lyu (Ed.), *Space weather study using*  
868 *multipoint techniques* (p. 127).
- 869 Chu, C., Zhang, H., Sibeck, D., Otto, A., Zong, Q., Omid, N., ... Angelopou-  
870 los, V. (2017, mar). THEMIS satellite observations of hot flow anoma-  
871 lies at Earth's bow shock. *Annales Geophysicae*, *35*(3), 443-451. doi:  
872 10.5194/angeo-35-443-2017
- 873 Cox, D. R., & Snell, E. J. (1970). *Analysis of Binary Data (2nd Edition)*. Chapman  
874 & Hall/CRC. doi: 10.1201/9781315137391
- 875 Dušík, Š., Granko, G., Šafránková, J., Němeček, Z., & Jelínek, K. (2010, oct). IMF  
876 cone angle control of the magnetopause location: Statistical study. *Geophysical*  
877 *Research Letters*, *37*(19), L19103. doi: 10.1029/2010GL044965
- 878 Eastwood, J. P., Lucek, E. A., Mazelle, C., Meziane, K., Narita, Y., Pickett, J., &  
879 Treumann, R. A. (2005, jun). The Foreshock. *Space Sci. Rev.*, *118*(1-4), 41-94.  
880 doi: 10.1007/s11214-005-3824-3
- 881 Elphic, R. C. (1995, jan). Observations of Flux Transfer Events: A Review. *Geo-*  
882 *physical Monograph Series*, *90*, 225. doi: 10.1029/GM090p0225
- 883 Escoubet, C. P., Fehringer, M., & Goldstein, M. (2001, oct). Introduction The Clus-  
884 ter mission. *Annales Geophysicae*, *19*, 1197-1200. doi: 10.5194/angeo-19-1197  
885 -2001
- 886 Fairfield, D. H. (1971, jan). Average and unusual locations of the Earth's magne-  
887 topause and bow shock. *Journal of Geophysical Research*, *76*(28), 6700. doi:  
888 10.1029/JA076i028p06700
- 889 Fairfield, D. H., Baumjohann, W., Paschmann, G., Luehr, H., & Sibeck, D. G.  
890 (1990, apr). Upstream pressure variations associated with the bow shock  
891 and their effects on the magnetosphere. *Journal of Geophysical Research*,  
892 *95*(A4), 3773-3786. doi: 10.1029/JA095iA04p03773
- 893 Friedman, J. H. (2001, oct). Greedy function approximation: A gradient boost-

- ing machine. *The Annals of Statistics*, 29(5), 1189 – 1232. Retrieved from <https://doi.org/10.1214/aos/1013203451> doi: 10.1214/aos/1013203451
- Géron, A. (2019). *Hands-on machine learning with Scikit-Learn, Keras, and TensorFlow: Concepts, tools, and techniques to build intelligent systems*. O'Reilly Media, Inc.
- Grimmich, N., Plaschke, F., Archer, M. O., Heyner, D., Mieth, J. Z. D., Nakamura, R., & Sibeck, D. G. (2023). *Database: THEMIS magnetopause crossings between 2007 and mid-2022* [dataset]. Open Science Framework (OSF). Retrieved from <https://osf.io/b6kux/> doi: 10.17605/OSF.IO/B6KUX
- Grygorov, K., Šafránková, J., Němeček, Z., Pi, G., Přech, L., & Urbář, J. (2017, nov). Shape of the equatorial magnetopause affected by the radial interplanetary magnetic field. *Planetary and Space Science*, 148, 28-34. doi: 10.1016/j.pss.2017.09.011
- Haaland, S., Hasegawa, H., Paschmann, G., Sonnerup, B., & Dunlop, M. (2021, aug). 20 Years of Cluster Observations: The Magnetopause. *Journal of Geophysical Research (Space Physics)*, 126(8), e29362. doi: 10.1029/2021JA029362
- Hasegawa, H. (2012, aug). Structure and Dynamics of the Magnetopause and Its Boundary Layers. *Monographs on Environment, Earth and Planets*, 1(2), 71-119. doi: 10.5047/meep.2012.00102.0071
- Henry, Z. W., Nykyri, K., Moore, T. W., Dimmock, A. P., & Ma, X. (2017, dec). On the Dawn-Dusk Asymmetry of the Kelvin-Helmholtz Instability Between 2007 and 2013. *Journal of Geophysical Research (Space Physics)*, 122(12), 11,888-11,900. doi: 10.1002/2017JA024548
- Howe, H. C., & Siscoe, G. L. (1972, jan). Magnetopause motions at lunar distance determined from the Explorer 35 Plasma Experiment. *Journal of Geophysical Research*, 77(31), 6071. doi: 10.1029/JA077i031p06071
- Jacobsen, K. S., Phan, T. D., Eastwood, J. P., Sibeck, D. G., Moen, J. I., Angelopoulos, V., ... Fornaçon, K. H. (2009, aug). THEMIS observations of extreme magnetopause motion caused by a hot flow anomaly. *Journal of Geophysical Research (Space Physics)*, 114(A8), A08210. doi: 10.1029/2008JA013873
- Johnson, J. R., Wing, S., & Delamere, P. A. (2014, nov). Kelvin Helmholtz Instability in Planetary Magnetospheres. *Space Sci. Rev.*, 184(1-4), 1-31. doi: 10.1007/s11214-014-0085-z
- Kavosi, S., & Raeder, J. (2015, may). Ubiquity of Kelvin-Helmholtz waves at Earth's magnetopause. *Nature Communications*, 6, 7019. doi: 10.1038/ncomms8019
- King, J. H., & Papitashvili, N. E. (2005, feb). Solar wind spatial scales in and comparisons of hourly Wind and ACE plasma and magnetic field data. *Journal of Geophysical Research (Space Physics)*, 110(A2), A02104. doi: 10.1029/2004JA010649
- Kuntz, K. D. (2019, jan). Solar wind charge exchange: an astrophysical nuisance. *The Astronomy and Astrophysics Review*, 27(1), 1. doi: 10.1007/s00159-018-0114-0
- LaMoury, A. T., Hietala, H., Plaschke, F., Vuorinen, L., & Eastwood, J. P. (2021, sep). Solar Wind Control of Magnetosheath Jet Formation and Propagation to the Magnetopause. *Journal of Geophysical Research (Space Physics)*, 126(9), e29592. doi: 10.1029/2021JA029592
- Larrodera, C., & Cid, C. (2020, mar). Bimodal distribution of the solar wind at 1 AU. *Astronomy and Astrophysics*, 635, A44. doi: 10.1051/0004-6361/201937307
- Lepping, R. P., Acuña, M. H., Burlaga, L. F., Farrell, W. M., Slavin, J. A., Schatten, K. H., ... Worley, E. M. (1995, feb). The Wind Magnetic Field Investigation. *Space Sci. Rev.*, 71(1-4), 207-229. doi: 10.1007/BF00751330

- 949 Lin, R. L., Zhang, X. X., Liu, S. Q., Wang, Y. L., & Gong, J. C. (2010, apr). A  
 950 three-dimensional asymmetric magnetopause model. *Journal of Geophysical*  
 951 *Research (Space Physics)*, *115*(A4), A04207. doi: 10.1029/2009JA014235
- 952 Liu, Z. Q., Lu, J. Y., Kabin, K., Yang, Y. F., Zhao, M. X., & Cao, X. (2012, jul).  
 953 Dipole tilt control of the magnetopause for southward IMF from global magne-  
 954 tohydrodynamic simulations. *Journal of Geophysical Research (Space Physics)*,  
 955 *117*(A7), A07207. doi: 10.1029/2011JA017441
- 956 Liu, Z. Q., Lu, J. Y., Wang, C., Kabin, K., Zhao, J. S., Wang, M., ... Zhao, M. X.  
 957 (2015, jul). A three-dimensional high Mach number asymmetric magnetopause  
 958 model from global MHD simulation. *Journal of Geophysical Research (Space*  
 959 *Physics)*, *120*(7), 5645-5666. doi: 10.1002/2014JA020961
- 960 Lu, J. Y., Liu, Z. Q., Kabin, K., Jing, H., Zhao, M. X., & Wang, Y. (2013, jun). The  
 961 IMF dependence of the magnetopause from global MHD simulations. *Journal*  
 962 *of Geophysical Research (Space Physics)*, *118*(6), 3113-3125. doi: 10.1002/jgra  
 963 .50324
- 964 Ma, X., Nykyri, K., Dimmock, A., & Chu, C. (2020, oct). Statistical Study of Solar  
 965 Wind, Magnetosheath, and Magnetotail Plasma and Field Properties: 12+  
 966 Years of THEMIS Observations and MHD Simulations. *Journal of Geophysical*  
 967 *Research (Space Physics)*, *125*(10), e28209. doi: 10.1029/2020JA028209
- 968 McComas, D. J., Bame, S. J., Barker, P., Feldman, W. C., Phillips, J. L., Riley,  
 969 P., & Griffee, J. W. (1998, jul). Solar Wind Electron Proton Alpha Monitor  
 970 (SWEPAM) for the Advanced Composition Explorer. *Space Sci. Rev.*, *86*,  
 971 563-612. doi: 10.1023/A:1005040232597
- 972 McFadden, J. P., Carlson, C. W., Larson, D., Ludlam, M., Abiad, R., Elliott,  
 973 B., ... Angelopoulos, V. (2008, dec). The THEMIS ESA Plasma Instru-  
 974 ment and In-flight Calibration. *Space Sci. Rev.*, *141*(1-4), 277-302. doi:  
 975 10.1007/s11214-008-9440-2
- 976 Merka, J., Szabo, A., Šafránková, J., & Němeček, Z. (2003, jul). Earth's bow shock  
 977 and magnetopause in the case of a field-aligned upstream flow: Observation  
 978 and model comparison. *Journal of Geophysical Research (Space Physics)*,  
 979 *108*(A7), 1269. doi: 10.1029/2002JA009697
- 980 Nguyen, G., Aunai, N., Michotte de Welle, B., Jeandet, A., Lavraud, B., & Fontaine,  
 981 D. (2022a, jan). Massive Multi-Mission Statistical Study and Analytical Mod-  
 982 eling of the Earth's Magnetopause: 1. A Gradient Boosting Based Automatic  
 983 Detection of Near-Earth Regions. *Journal of Geophysical Research (Space*  
 984 *Physics)*, *127*(1), e29773. doi: 10.1029/2021JA029773
- 985 Nguyen, G., Aunai, N., Michotte de Welle, B., Jeandet, A., Lavraud, B., &  
 986 Fontaine, D. (2022b, jan). Massive Multi-Mission Statistical Study and  
 987 Analytical Modeling of the Earth's Magnetopause: 2. Shape and Location.  
 988 *Journal of Geophysical Research (Space Physics)*, *127*(1), e29774. doi:  
 989 10.1029/2021JA029774
- 990 Nguyen, G., Aunai, N., Michotte de Welle, B., Jeandet, A., Lavraud, B., & Fontaine,  
 991 D. (2022c, jan). Massive Multi-Mission Statistical Study and Analytical  
 992 Modeling of the Earth's Magnetopause: 3. An Asymmetric Non Indented Mag-  
 993 netopause Analytical Model. *Journal of Geophysical Research (Space Physics)*,  
 994 *127*(1), e30112. doi: 10.1029/2021JA030112
- 995 Ogilvie, K. W., Chornay, D. J., Fritzenreiter, R. J., Hunsaker, F., Keller, J., Lo-  
 996 bell, J., ... Gergin, E. (1995, feb). SWE, A Comprehensive Plasma In-  
 997 strument for the Wind Spacecraft. *Space Sci. Rev.*, *71*(1-4), 55-77. doi:  
 998 10.1007/BF00751326
- 999 Olshevsky, V., Khotyaintsev, Y. V., Lalti, A., Divin, A., Delzanno, G. L., Anderzén,  
 1000 S., ... Markidis, S. (2021, oct). Automated Classification of Plasma Regions  
 1001 Using 3D Particle Energy Distributions. *Journal of Geophysical Research*  
 1002 *(Space Physics)*, *126*(10), e29620. doi: 10.1029/2021JA029620
- 1003 Panov, E. V., Büchner, J., Fränz, M., Korth, A., Savin, S. P., Rème, H., &

- 1004       Fornaçon, K. H. (2008, jan). High-latitude Earth’s magnetopause outside the  
1005       cusp: Cluster observations. *Journal of Geophysical Research (Space Physics)*,  
1006       113(A1), A01220. doi: 10.1029/2006JA012123
- 1007       Park, J.-S., Shue, J.-H., Kim, K.-H., Pi, G., Němeček, Z., & Šafránková, J. (2016,  
1008       jul). Global expansion of the dayside magnetopause for long-duration radial  
1009       IMF events: Statistical study on GOES observations. *Journal of Geophysical*  
1010       *Research (Space Physics)*, 121(7), 6480-6492. doi: 10.1002/2016JA022772
- 1011       Pedregosa, F., Varoquaux, G., Gramfort, A., Michel, V., Thirion, B., Grisel, O., ...  
1012       Duchesnay, E. (2011). Scikit-learn: Machine Learning in Python. *Journal of*  
1013       *Machine Learning Research*, 12, 2825–2830.
- 1014       Plaschke, F., Glassmeier, K. H., Auster, H. U., Angelopoulos, V., Constantinescu,  
1015       O. D., Fornaçon, K. H., ... Nakamura, R. (2009, jan). Statistical study of the  
1016       magnetopause motion: First results from THEMIS. *Journal of Geophysical*  
1017       *Research (Space Physics)*, 114, A00C10. doi: 10.1029/2008JA013423
- 1018       Plaschke, F., Glassmeier, K. H., Auster, H. U., Constantinescu, O. D., Magnes, W.,  
1019       Angelopoulos, V., ... McFadden, J. P. (2009, jan). Standing Alfvén waves  
1020       at the magnetopause. *Geophysical Research Letters*, 36(2), L02104. doi:  
1021       10.1029/2008GL036411
- 1022       Plaschke, F., Hietala, H., & Angelopoulos, V. (2013, oct). Anti-sunward high-speed  
1023       jets in the subsolar magnetosheath. *Annales Geophysicae*, 31(10), 1877-1889.  
1024       doi: 10.5194/angeo-31-1877-2013
- 1025       Plaschke, F., Hietala, H., Archer, M., Blanco-Cano, X., Kajdič, P., Karlsson, T., ...  
1026       Sibeck, D. (2018, aug). Jets Downstream of Collisionless Shocks. *Space Sci.*  
1027       *Rev.*, 214(5), 81. doi: 10.1007/s11214-018-0516-3
- 1028       Plaschke, F., Hietala, H., & Vörös, Z. (2020, sep). Scale Sizes of Magnetosheath  
1029       Jets. *Journal of Geophysical Research (Space Physics)*, 125(9), e27962. doi: 10  
1030       .1029/2020JA027962
- 1031       Raab, W., Branduardi-Raymont, G., Wang, C., Dai, L., Donovan, E., Enno, G.,  
1032       ... Zheng, J. (2016, jul). SMILE: a joint ESA/CAS mission to investigate  
1033       the interaction between the solar wind and Earth’s magnetosphere. In J.-  
1034       W. A. den Herder, T. Takahashi, & M. Bautz (Eds.), *Space telescopes and*  
1035       *instrumentation 2016: Ultraviolet to gamma ray* (Vol. 9905, p. 990502). doi:  
1036       10.1117/12.2231984
- 1037       Russell, C. T., Petrinec, S. M., Zhang, T. L., Song, P., & Kawano, H. (1997, jun).  
1038       The effect of foreshock on the motion of the dayside magnetopause. *Geophys-*  
1039       *ical Research Letters*, 24(12), 1439-1441. doi: 10.1029/97GL01408
- 1040       Safránková, J., Nemecek, Z., Dusík, S., Prech, L., Sibeck, D. G., & Borodkova, N. N.  
1041       (2002, mar). The magnetopause shape and location: a comparison of the In-  
1042       terball and Geotail observations with models. *Annales Geophysicae*, 20(3),  
1043       301-309. doi: 10.5194/angeo-20-301-2002
- 1044       Samsonov, A. A., Němeček, Z., Šafránková, J., & Jelínek, K. (2012, may). Why does  
1045       the subsolar magnetopause move sunward for radial interplanetary magnetic  
1046       field? *Journal of Geophysical Research (Space Physics)*, 117(A5), A05221. doi:  
1047       10.1029/2011JA017429
- 1048       Shue, J. H., & Chao, J. K. (2013, jun). The role of enhanced thermal pressure in  
1049       the earthward motion of the Earth’s magnetopause. *Journal of Geophysical*  
1050       *Research (Space Physics)*, 118(6), 3017-3026. doi: 10.1002/jgra.50290
- 1051       Shue, J. H., Chao, J. K., Fu, H. C., Russell, C. T., Song, P., Khurana, K. K., &  
1052       Singer, H. J. (1997, may). A new functional form to study the solar wind  
1053       control of the magnetopause size and shape. *Journal of Geophysical Research*,  
1054       102(A5), 9497-9512. doi: 10.1029/97JA00196
- 1055       Shue, J. H., Chao, J. K., Song, P., McFadden, J. P., Suvorova, A., Angelopoulos, V.,  
1056       ... Plaschke, F. (2009, sep). Anomalous magnetosheath flows and distorted  
1057       subsolar magnetopause for radial interplanetary magnetic fields. *Geophysical*  
1058       *Research Letters*, 36(18), L18112. doi: 10.1029/2009GL039842

- 1059 Shue, J. H., Song, P., Russell, C. T., Steinberg, J. T., Chao, J. K., Zastenker, G.,  
 1060 ... Kawano, H. (1998, aug). Magnetopause location under extreme solar  
 1061 wind conditions. *Journal of Geophysical Research*, *103*(A8), 17691-17700. doi:  
 1062 10.1029/98JA01103
- 1063 Sibeck, D. G., Allen, R., Aryan, H., Bodewits, D., Brandt, P., Branduardi-Raymont,  
 1064 G., ... Wing, S. (2018, jun). Imaging Plasma Density Structures in the Soft  
 1065 X-Rays Generated by Solar Wind Charge Exchange with Neutrals. *Space Sci.*  
 1066 *Rev.*, *214*(4), 79. doi: 10.1007/s11214-018-0504-7
- 1067 Sibeck, D. G., Borodkova, N. L., Schwartz, S. J., Owen, C. J., Kessel, R., Kokubun,  
 1068 S., ... Zastenker, G. N. (1999, mar). Comprehensive study of the magne-  
 1069 toospheric response to a hot flow anomaly. *Journal of Geophysical Research*,  
 1070 *104*(A3), 4577-4594. doi: 10.1029/1998JA900021
- 1071 Sibeck, D. G., Lopez, R. E., & Roelof, E. C. (1991, apr). Solar wind control of the  
 1072 magnetopause shape, location, and motion. *Journal of Geophysical Research*,  
 1073 *96*(A4), 5489-5495. doi: 10.1029/90JA02464
- 1074 Slavin, J. A., Szabo, A., Peredo, M., Lepping, R. P., Fitzenreiter, R. J., Ogilvie,  
 1075 K. W., ... Steinberg, J. T. (1996, may). Near-simultaneous bow shock cross-  
 1076 ings by WIND and IMP 8 on December 1, 1994. *Geophysical Research Letters*,  
 1077 *23*(10), 1207-1210. doi: 10.1029/96GL01351
- 1078 Smith, C. W., L'Heureux, J., Ness, N. F., Acuña, M. H., Burlaga, L. F., & Scheifele,  
 1079 J. (1998, jul). The ACE Magnetic Fields Experiment. *Space Sci. Rev.*, *86*,  
 1080 613-632. doi: 10.1023/A:1005092216668
- 1081 Staples, F. A., Rae, I. J., Forsyth, C., Smith, A. R. A., Murphy, K. R., Raymer,  
 1082 K. M., ... Imber, S. M. (2020, apr). Do Statistical Models Capture the  
 1083 Dynamics of the Magnetopause During Sudden Magnetospheric Compres-  
 1084 sions? *Journal of Geophysical Research (Space Physics)*, *125*(4), e27289. doi:  
 1085 10.1029/2019JA027289
- 1086 Stone, E. C., Frandsen, A. M., Mewaldt, R. A., Christian, E. R., Margolies, D.,  
 1087 Ormes, J. F., & Snow, F. (1998, jul). The Advanced Composition Explorer.  
 1088 *Space Sci. Rev.*, *86*, 1-22. doi: 10.1023/A:1005082526237
- 1089 Suvorova, A. V., & Dmitriev, A. V. (2015, apr). Magnetopause inflation under ra-  
 1090 dial IMF: Comparison of models. *Earth and Space Science*, *2*(4), 107-114. doi:  
 1091 10.1002/2014EA000084
- 1092 Suvorova, A. V., Shue, J. H., Dmitriev, A. V., Sibeck, D. G., McFadden, J. P.,  
 1093 Hasegawa, H., ... Němeček, Z. (2010, oct). Magnetopause expansions for  
 1094 quasi-radial interplanetary magnetic field: THEMIS and Geotail observations.  
 1095 *Journal of Geophysical Research (Space Physics)*, *115*(A10), A10216. doi:  
 1096 10.1029/2010JA015404
- 1097 Tátrallyay, M., Erdős, G., Németh, Z., Verigin, M. I., & Vennerstrom, S. (2012,  
 1098 dec). Multispacecraft observations of the terrestrial bow shock and magne-  
 1099 topause during extreme solar wind disturbances. *Annales Geophysicae*, *30*(12),  
 1100 1675-1692. doi: 10.5194/angeo-30-1675-2012
- 1101 Taylor, M. G. G. T., Hasegawa, H., Lavraud, B., Phan, T., Escoubet, C. P., Dun-  
 1102 lop, M. W., ... Wild, J. A. (2012, jun). Spatial distribution of rolled up  
 1103 Kelvin-Helmholtz vortices at Earth's dayside and flank magnetopause. *Annales*  
 1104 *Geophysicae*, *30*(6), 1025-1035. doi: 10.5194/angeo-30-1025-2012
- 1105 Treumann, R. A. (2009, dec). Fundamentals of collisionless shocks for astrophysical  
 1106 application, 1. Non-relativistic shocks. *The Astronomy and Astrophysics Re-*  
 1107 *view*, *17*(4), 409-535. doi: 10.1007/s00159-009-0024-2
- 1108 Turner, D. L., Eriksson, S., Phan, T. D., Angelopoulos, V., Tu, W., Liu, W., ...  
 1109 Glassmeier, K. H. (2011, apr). Multispacecraft observations of a foreshock-  
 1110 induced magnetopause disturbance exhibiting distinct plasma flows and an  
 1111 intense density compression. *Journal of Geophysical Research (Space Physics)*,  
 1112 *116*(A4), A04230. doi: 10.1029/2010JA015668
- 1113 Turner, D. L., Omidi, N., Sibeck, D. G., & Angelopoulos, V. (2013, apr). First ob-

- 1114 observations of foreshock bubbles upstream of Earth's bow shock: Characteristics  
 1115 and comparisons to HFAs. *Journal of Geophysical Research (Space Physics)*,  
 1116 *118*(4), 1552-1570. doi: 10.1002/jgra.50198
- 1117 Vu, A., Liu, T. Z., Zhang, H., & Pollock, C. (2022, feb). Statistical Study of Fore-  
 1118 shock Bubbles, Hot Flow Anomalies, and Spontaneous Hot Flow Anomalies  
 1119 and Their Substructures Observed by MMS. *Journal of Geophysical Research*  
 1120 *(Space Physics)*, *127*(2), e2021JA030029. doi: 10.1029/2021JA030029
- 1121 Walsh, A. P., Haaland, S., Forsyth, C., Keesee, A. M., Kissinger, J., Li, K., ... Tay-  
 1122 lor, M. G. G. T. (2014, jul). Dawn-dusk asymmetries in the coupled solar  
 1123 wind-magnetosphere-ionosphere system: a review. *Annales Geophysicae*, *32*(7),  
 1124 705-737. doi: 10.5194/angeo-32-705-2014
- 1125 Wang, C., & Sun, T. (2022, dec). Methods to derive the magnetopause from soft X-  
 1126 ray images by the SMILE mission. *Geoscience Letters*, *9*(1), 30. doi: 10.1186/  
 1127 s40562-022-00240-z
- 1128 Wang, M., Lu, J. Y., Kabin, K., Yuan, H. Z., Zhou, Y., & Guan, H. Y. (2020,  
 1129 may). Influence of the Interplanetary Magnetic Field Cone Angle on the  
 1130 Geometry of Bow Shocks. *The Astronomical Journal*, *159*(5), 227. doi:  
 1131 10.3847/1538-3881/ab86a7
- 1132 Winterhalter, D., & Kivelson, M. G. (1988, sep). Observations of the Earth's bow  
 1133 shock under high Mach number/high plasma beta solar wind conditions. *Geo-  
 1134 physical Research Letters*, *15*(10), 1161-1164. doi: 10.1029/GL015i010p01161
- 1135 Zhang, H., Zong, Q., Connor, H., Delamere, P., Facskó, G., Han, D., ... Yao,  
 1136 S. (2022, aug). Dayside Transient Phenomena and Their Impact on  
 1137 the Magnetosphere and Ionosphere. *Space Sci. Rev.*, *218*(5), 40. doi:  
 1138 10.1007/s11214-021-00865-0
- 1139 Zhang, L. Q., Wang, C., Wang, J. Y., & Lui, A. T. Y. (2019, may). Statistical  
 1140 properties of the IMF clock angle in the solar wind with northward and south-  
 1141 ward interplanetary magnetic field based on ACE observation from 1998 to  
 1142 2009: Dependence on the temporal scale of the solar wind. *Advances in Space  
 1143 Research*, *63*(10), 3077-3087. doi: 10.1016/j.asr.2019.01.023